# Development of a Trans-dimensional Fault Slip Inversion for Geodetic Data

**F. Tomita[1], T. Iinuma[1], R. Agata[1], T. Hori[1]**

[1]Research Institute for Marine Geodynamics, Japan Agency for Marine-Earth Science and Technology

Corresponding author: Fumiaki Tomita (tomitaf@jamstec.go.jp)

†Additional author notes should be indicated with symbols (current addresses, for example).

**Key Points:**

- Trans-dimensional geodetic inversion method was developed and applied to synthetic tests and data for the 2011 Tohoku-oki earthquake
- The developed method can express a spatially non-uniform slip distribution and uncertainties for unknowns following non-Gaussian distributions
- The developed method can appropriately adjust scaling factors for the observational errors

## Abstract

Geodetic fault slip inversions have been generally performed by employing a least squares method with a spatial smoothing constraint. However, this conventional method has various problems: difficulty in strictly estimating non-negative solutions, assumption that unknowns follow the Gaussian distributions, unsuitability for expressing spatially non-uniform slip distributions, and high calculation cost for optimizing many hyper-parameters. Here, we have developed a trans-dimensional geodetic slip inversion method using the reversible-jump Markov chain Monte Carlo (rj-MCMC) technique to overcome the problems. Because sub-fault locations were parameterized by the Voronoi partition and were optimized in our approach, we can estimate a slip distribution without the spatial smoothing constraint. Moreover, we introduced scaling factors for observational errors. We applied the method to the synthetic data and the actual geodetic observational data associated with the 2011 Tohoku-oki earthquake and found that the method successfully reproduced the target slip distributions including a spatially non-uniform slip distribution. The method provided posterior probability distributions with the unknowns, which can express a non-Gaussian distribution such as large slip with low probability. The estimated scaling factors properly adjusted the initial observational errors and provided a reasonable slip distribution. Additionally, we found that checkerboard resolution tests were useful to consider sensitivity of the observational data for performing the rj-MCMC method. It is concluded that the developed method is a powerful technique to solve the problems of the conventional inversion method and to flexibly express fault-slip distributions considering the complicated uncertainties.


## 1 Introduction

Precise estimation on fault slip distributions is important to understand slip behaviors during earthquake cycles. Geodetic slip inversions have been generally conducted to estimate fault slip distributions, and a conventional geodetic slip inversion is performed by a least squares method (LSM). In this conventional approach, a smoothing constraint on fault-slips (e.g., Laplacian regulation) is generally provided to avoid overfitting. Then, strength of smoothing is determined by a criteria such as a trade-off L-curve [e.g., Du et al., 1992] and Akaike's Bayesian

Information Criterion (ABIC) [e.g., Yabuki & Matsu'ura, 1992]. However, some problems in the LSM-based geodetic slip inversion have been noted: (1) it is difficult to strictly impose a direct constraint (such as non-negative constraint) [Fukuda & Johnson, 2008], (2) it is difficult to evaluate estimation error when unknowns follow non-Gaussian distributions, (3) it is unsuitable for estimating a spatially heterogeneous fault slip distribution because spatially uniform smoothing is applied, and (4) it takes effort to adjust the hyper-parameters when the multiple hyper-parameters are introduced, such as weighting hyper-parameters for multiple data and smoothing hyper-parameters for multiple time-windows in the viscoelastic inversion [Tomita et al., 2020].

To overcome the above problems, various approaches have been developed. Although LSMs without using the simple Laplacian regulation have been investigated, such as utilizing spectral decomposition [e.g., Hori, 2001; Jin et al., 2007; Xu et al., 2018] and promoting sparse solutions [e.g., Evans & Meade, 2012], they are not suitable for solving problems (1) and (2). Meanwhile, slip inversion methods using a Markov chain Monte Carlo (MCMC) technique have been well developed recently [e.g., Fukuda & Johnson, 2008; Minson et al., 2013]. MCMC-based slip inversions can treat a direct constraint strictly and express posterior probability distributions of model parameters [Fukuda & Johnson, 2008]. Furthermore, they can provide posterior probability distributions of hyper-parameters as well as those of the model parameters [e.g., Fukuda & Johnson, 2008; Kubo et al., 2016], which is an useful solution for the problem (4). Thus, MCMC is a useful technique to solve the problems (1), (2), and (3). Although most of the previous MCMC-based slip inversion studies have introduced the Laplacian regulation as similar to the LSM-based slip inversions, MCMC-based slip inversions without using the Laplacian regulation have been recently developed to solve the problem (3). One approach is that the number and size of sub-faults are optimized based on the spatial resolution of observational data prior to the MCMC sampling [Kimura et al., 2019]; however, a spatially smooth fault slip distribution cannot be resolved by this method. Another idea is introduction of a complicated regulation such as von Karman regulation [e.g., Amey et al., 2018].

Here, we investigated a trans-dimensional geodetic slip inversion method using a reversible jump MCMC (rj-MCMC) technique [Green, 1995]. Through the trans-dimensional approach, number of model parameters is automatically adjusted based on the sensitivity of observational data and model complexity. Among the applications of the trans-dimensional

approach to geophysics [e.g., Bodin & Sambridge, 2009; Hawkins & Sambridge, 2015], spatial model parameters are divided into groups by a parameterization technique (e.g., Voronoi partition, Figure 1). For the Voronoi partition parameterization, model space is discretized using the Voronoi nuclei (Figure 1), and number and spatial positions of the nuclei are optimized through rj-MCMC sampling [Bodin and Sambridge, 2009]. Considering this optimization, the trans-dimensional approach can be regarded as a sparse modeling method. As indicated by Bodin and Sambridge [2009], ensemble of the rj-MCMC samples can express spatially smooth distribution of the model parameters without any smoothing constraints. Furthermore, weighting hyper-parameters for multiple observation data can be introduced in the rj-MCMC technique in the same manner as conventional MCMC techniques [e.g., Dettmer et al., 2014]. Thus, we expect that the trans-dimensional approach overcomes all of the above problems.

For geophysical studies, the trans-dimensional approach has been often applied to explore underground geophysical structures using seismic wave data [e.g., Bodin & Sambridge, 2009; Bodin et al. 2012] and electrical resistivity data [e.g., Galetti & Curtis 2018]. Furthermore, the approach has been also applied to estimate tsunami sources due to a large subduction earthquake [Dettmer et al., 2016]. However, there are few applications of the approach to estimate fault slip distributions; for example, Dettmer et al. [2014] and Hallo and Gallovič [2020] investigated a fault slip distribution using seismic wave data. Although Amey et al. [2019] estimated a fault slip distribution using geodetic observational data, they utilized the rj-MCMC technique and a von Karman regulation together to restrict the number of sub-faults with non-zero slip. Thus, the application of the trans-dimensional geodetic slip inversion has not been well investigated.

One of the chracteristics of the geodetic slip inversion is that we often treat many types of observational data such as onland GNSS, onland InSAR, offshore GNSS-Acoustic (GNSS-A), offshore bottom pressure (OBP), and the others. Determination of relative weights among these various data is an important issue [e.g., Funning et al., 2014]; however, it is difficult optimized the relative weights by conventional inversion approaches because of computational costs when types of the observational data are many. This study tried to automalltically adjust many weighting hyper-parameters through the MCMC sampling process. Moreover, compared with other geophysical data, the geodetic data have heterogeneity of spatial coverage of observational sites: dense onshore sites and sparse offshore sites. This heterogeneity provides strong spatial variation of sensitivity to fault slips. We expect thet the rj-MCMC method can consider such

spatil variation of the data sensitivity because fault patch sizes are variable depending on the observational data. Thus, this study tried investigated how the rj-MCMC method works for various patterns of the observational sites.

In this study, we performed a simple trans-dimensional geodetic slip inversion using the rj-MCMC method based on the Voronoi partition through synthetic tests and an application to actual observational data associated with the 2011 Tohoku-oki earthquake. We then assessed utility of the trans-dimensional inversion approach for analyzing geodetic observational data.

## 2 Methods

### 2.1 Observation equation

We aim to analyze geodetic observational data with multiple time windows or from multiple observational instruments. An observational equation that links the vector of ground surface displacements $\mathbf{d}$ with the vector of fault slips $\mathbf{s}$ via the matrix of Green's functions $\mathbf{G}$ is:

$$\mathbf{d} = \mathbf{G}\mathbf{s} + \mathbf{e}, \tag{1}$$

where $\mathbf{e}$ is an observational error vector. When we have I types of the observational data and J components of fault slips (hereafter, called as fault-slip component), Equation (1) is re-written as follows:

$$\begin{pmatrix} \mathbf{d}_1 \\ \vdots \\ \mathbf{d}_I \end{pmatrix} = \begin{pmatrix} \mathbf{G}_{1,1} & \cdots & \mathbf{G}_{1,J} \\ \vdots & \ddots & \vdots \\ \mathbf{G}_{I,1} & \cdots & \mathbf{G}_{I,J} \end{pmatrix} \begin{pmatrix} \mathbf{s}_1 \\ \vdots \\ \mathbf{s}_J \end{pmatrix} + \begin{pmatrix} \mathbf{e}_1 \\ \vdots \\ \mathbf{e}_I \end{pmatrix}; \tag{2}$$

for example, if we estimate fault slips in horizontally orthogonal slip directions for coseismic slip, $J = 2$, or if we estimate fault slips in horizontally orthogonal slip directions for transient slip with three time windows, $J = 2 \times 3$.

We consider the observational error vector $\mathbf{e}$ obeys an observational covariance matrix $\mathbf{E}$. The observational covariance matrix can be expressed by combination of $I$ types of the observational covariance matrices $\mathbf{E}_i (i = 1, \cdots, I)$ as

$$\mathbf{e} \sim \mathbf{E} = \begin{pmatrix} \mathbf{E}_1 & \square & \mathbf{0} \\ \square & \ddots & \square \\ \mathbf{0} & \square & \mathbf{E}_I \end{pmatrix}. \tag{3}$$

Most of the previous geodetic inversion studies fixed the observational covariance matrix initially given from instrumental measurement errors. However, considering modeling errors and the difficulty in assessing instrumental measurement errors, it is reasonable to introduce scale factors to the individual types of the observational covariance matrices [e.g., Dettmer et al., 2014; Funning et al., 2014]. According to Dettmer et al. [2014], we provided hierarchical scaling parameters, $\lambda_i^2 (i = 1, \cdots, I)$, which multiplies the initial observational covariance matrices $\mathbf{E}_i^{\mathrm{ini}} (i = 1, \cdots, I)$. As each hierarchical scaling parameter is a positive value, we transformed $\lambda_i^2$ into $10^{-\Lambda_i}$ and sampled $\Lambda_i (i = 1, \cdots, I)$ in same manner as Kubo et al. [2016] (hereafter, $\Lambda$ is called as a weighting parameter). Then, Equation (3) is re-written as

$$\mathbf{e} \sim \mathbf{E} = \begin{pmatrix} \mathbf{E}_1 & \cdots & \mathbf{0} \\ \vdots & \ddots & \vdots \\ \mathbf{0} & \cdots & \mathbf{E}_I \end{pmatrix} = \begin{pmatrix} \lambda_1^2 \mathbf{E}_1^{\mathrm{ini}} & \cdots & \mathbf{0} \\ \vdots & \ddots & \vdots \\ \mathbf{0} & \cdots & \lambda_I^2 \mathbf{E}_I^{\mathrm{ini}} \end{pmatrix} = \begin{pmatrix} 10^{-\Lambda_1} \mathbf{E}_1^{\mathrm{ini}} & \cdots & \mathbf{0} \\ \vdots & \ddots & \vdots \\ \mathbf{0} & \cdots & 10^{-\Lambda_I} \mathbf{E}_I^{\mathrm{ini}} \end{pmatrix}. \tag{4}$$

Subseqently, defining $\mathbf{W}_i^{\mathrm{ini}} = {\mathbf{E}^{\mathrm{ini}}}_i^{-1}$, the weight matrix is written as

$$\boldsymbol{W} = \begin{pmatrix} 10^{\Lambda_1} \mathbf{W}_1^{\mathrm{ini}} & \cdots & \mathbf{0} \\ \vdots & \ddots & \vdots \\ \mathbf{0} & \cdots & 10^{\Lambda_I} \mathbf{W}_I^{\mathrm{ini}} \end{pmatrix}. \tag{5}$$

## 2.2 Principle of the rj-MCMC method

In the Bayesian framework, all information on unknowns can be expressed by the probability density function (PDF). From Bayes theorem [Bayes, 1763], a posterior PDF of unknowns $\mathbf{x}$ when data $\mathbf{d}$ are given can be written as

$$p(\mathbf{x} \mid \mathbf{d}) = \frac{p(\mathbf{d} \mid \mathbf{x}) p(\mathbf{x})}{p(\mathbf{d})} \propto p(\mathbf{d} \mid \mathbf{x}) p(\mathbf{x}) \tag{6}$$

where $p(\mathbf{d} \mid \mathbf{x})$ is a likelihood function of observational data $\mathbf{d}$ given $\mathbf{x}$, and $p(\mathbf{x})$ is the a priori PDF of $\mathbf{x}$. The posterior PDF can be written by a proportionality relationship using $p(\mathbf{d} \mid \mathbf{x})$ and $p(\mathbf{x})$ because $p(\mathbf{d})$, which is evidence indicating a priori PDF of $\mathbf{d}$, is independent of $\mathbf{x}$ [e.g., Sambridge et al., 2006]. In an ordinary MCMC approach (e.g., the Metropolis-Hasting (MH) algorithm [Metropolis et al., 1953; Hastings, 1970]), unknowns are updated based on a posterior PDF. As for the MH algorithm, unknown candidates $\mathbf{x}'$ are generated from current unknowns $\boldsymbol{x}$ by adding perturbation based on a proposal distribution (e.g., uniform or normal distribution).

153 Then, an acceptance probability $\alpha_{MH}$ is calculated as a ratio of the posterior PDFs when proposal
154 PDFs $q(\mathbf{x}' \mid \mathbf{x})$ and $q(\mathbf{x} \mid \mathbf{x}')$ are symmetric [e.g., Fukuda & Johnson, 2008; Kubo et al., 2016]:

$$\alpha_{\mathrm{MH}}(\mathbf{x}' \mid \mathbf{x}) = \min\left[1, \frac{p(\mathbf{x}' \mid \mathbf{d})}{p(\mathbf{x} \mid \mathbf{d})} \times \frac{q(\mathbf{x} \mid \mathbf{x}')}{q(\mathbf{x}' \mid \mathbf{x})}\right] \propto \min\left[1, \frac{p(\mathbf{x}' \mid \mathbf{d})}{p(\mathbf{x} \mid \mathbf{d})}\right]. \quad (7)$$

155 If $\alpha_{\mathrm{MH}} > u$ ($u$ is a random number generated from a uniform distribution with a range between 0
156 and 1), the candidates are accepted. The unknown values are sampled during iterative updates of
157 the unknowns based on the above process; the ensemble of the sampled unknown values
158 demonstrates the estimates of the unknowns following their posterior PDFs.

159 For the rj-MCMC approach, an extended form of the acceptance probability in the MH
160 algorithm has been generally utilized, which was implemented as the Metropolis-Hasting-Green
161 (MHG) algorithm [Green, 1995; 2003]. The acceptance probability in the MHG algorithm is
162 written as

$$\alpha_{\mathrm{MHG}}(\mathbf{x}' \mid \mathbf{x}) = \min\left[1, \frac{p(\mathbf{x}' \mid \mathbf{d})}{p(\mathbf{x} \mid \mathbf{d})} \times \frac{q(\mathbf{x} \mid \mathbf{x}')}{q(\mathbf{x}' \mid \mathbf{x})} \times |\mathbf{J}|\right] \quad (8)$$

163 where $\mathbf{J}$ is the Jacobian for the transformation from $\mathbf{x}$ to $\mathbf{x}'$, which evaluates the scale changes
164 due to a dimensional jump between $\mathbf{x}$ and $\mathbf{x}'$. However, we can simply consider $|\mathbf{J}| = 1$ when the
165 transformed dimension is less than one, such as in a case of the birth/death rj-MCMC method
166 [e.g., Denison et al., 2002; Bodin & Sambridge, 2009]. In this study, we employed the
167 birth/death rj-MCMC method. The details of the birth/death rj-MCMC method are denoted in
168 Section 2-4. Thus, considering Equation (6), the acceptance probability in this study can be
169 expressed as following:

$$\begin{aligned} \alpha(\mathbf{x}' \mid \mathbf{x}) &= \min[1, (\textbf{prior ratio}) \times (\textbf{likelihood ratio}) \times (\textbf{proposal ratio})] \quad (9) \\ &= \min\left[1, \frac{p(\mathbf{x}')}{p(\mathbf{x})} \times \frac{p(\mathbf{d} \mid \mathbf{x}')}{p(\mathbf{d} \mid \mathbf{x})} \times \frac{q(\mathbf{x} \mid \mathbf{x}')}{q(\mathbf{x}' \mid \mathbf{x})}\right]. \end{aligned}$$

170 Like the ordinary MCMC, the unknowns are updated based on the acceptance probability
171 and are sampled. The practical implementation of the dimensional jump and of the unknowns'
172 update is denoted later.

173

## 2.3 Parameterization of unknowns

We introduced a set of the Voronoi nuclei to discretize a 2-dimensional fault plane as shown in Figure 1. The fault plane is covered by sub-faults (black rectangles). Each sub-fault was classified by distance from the Voronoi nuclei (red circles); this classification demonstrated the Voronoi cells (colors of sub-faults). The Voronoi nuclei are generated from a nucleus grid (gray dots). The total number of nucleus grid points is defined as $K^{\mathrm{grid}}$. Using the Voronoi partition, the unknowns expressing fault slip distributions are defined as the combination of locations of the Voronoi nuclei $\mathbf{c}$ and slips for individual cells $\overline{\mathbf{s}}$. Note that the slips $\overline{\mathbf{s}}$ are defined as a partitioned form of $\mathbf{s}$. Defining the number of the Voronoi nuclei for the $j$th fault-slip component is $K_j$, the unknown vector for the locations of the Voronoi nuclei $\mathbf{c}$ can be written as

$$\mathbf{c} = \begin{pmatrix} \mathbf{c}_1 \\ \vdots \\ \mathbf{c}_J \end{pmatrix} = \begin{pmatrix} c_{1_1} \\ \vdots \\ c_{K_J} \end{pmatrix}. \tag{10}$$

Note that each nucleus location $c_{k_j}$ denotes a locational number of the nucleus grid; the locational number is assigned for each point of the nucleus grid in advance. The unknown vector for the slips $\overline{\mathbf{s}}$ can be written as

$$\overline{\mathbf{s}} = \begin{pmatrix} \overline{\mathbf{s}}_1 \\ \vdots \\ \overline{\mathbf{s}}_J \end{pmatrix} = \begin{pmatrix} \overline{s}_{1_1} \\ \vdots \\ \overline{s}_{K_J} \end{pmatrix}. \tag{11}$$

Besides the unknowns expressing fault slip distributions, the number of the Voronoi nuclei and the weighting parameters also account for unknowns. Defining the number of the Voronoi nuclei for the $j$th fault-slip component is $K_j$, the unknown vector for number of the Voronoi nuclei is expressed as $\mathbf{k} = (K_1, \cdots, K_J)$. Furthermore, the unknown vector for the weighting parameters is defined as $\mathbf{h} = (\Lambda_1, \cdots, \Lambda_I)$. Thus, the unknown vector can be finally written as

$$\mathbf{x} = \begin{pmatrix} \mathbf{k} \\ \mathbf{h} \\ \mathbf{c} \\ \overline{\mathbf{s}} \end{pmatrix}. \tag{12}$$

## 2.4 Birth/death rj-MCMC algorithm

We summarized our birth/death rj-MCMC algorithm as a flowchart in Figure S2. Based on Bodin and Sambridge [2009] and Galetti and Curtis [2018], we iteratively optimized the unknowns from initial values by following three steps: (1) "slip update" updating the slip amount for a randomly chosen Voronoi cell $\overline{s}_{k_j}$; (2) "weight update" updating the weighting parameters $\mathbf{h}$; (3) "Voronoi partition update" updating the number of the Voronoi nuclei $\mathbf{k}$, the locations of the Voronoi nuclei $\mathbf{c}$, and the corresponding slip $\overline{\mathbf{s}}$.

In the step (1), we randomly chose the $k$th Voronoi cell of the $j$th fault-slip component with the slip of $\overline{s}_{k_j}$. According to Bodin and Sambridge [2009], we generated a new candidate of the slip parameter $\overline{s}'_{k_j}$ as following:

$$\overline{s}'_{k_j} = \overline{s}_{k_j} + v\sigma_{\text{slip}} \tag{13}$$

where $v$ is a random coefficient derived from a normal distribution $N(0,1)$ and $\sigma_{\text{slip}}$ is a constant denoting the standard deviation of the proposal PDF for the slip. This step is same with the ordinary MH algorithm and does not involve a dimensional jump.

In the step (2), we generated a new candidate of the weighting parameters $\mathbf{h}'$ as

$$\mathbf{h}' = \mathbf{h} + \sigma_{\text{scale}}\mathbf{v}, \tag{14}$$

where $\mathbf{v}$ is a random coefficient vector ($I$ dimensions) derived from a normal distribution $N(0,1)$ and $\sigma_{\text{scale}}$ is a constant denoting the standard deviation of the proposal PDF for the weighting parameters. This step is also same the ordinary MH algorithm and does not involve a dimensional jump.

We implemented the birth/death algorithm in step (3). According to Bodin and Sambridge [2009], we performed this step only at every odd iteration loop. Step (3) branches into three actions: (a) "birth" action that adds a new nucleus is added, (b) "death" action that chooses one nucleus randomly from the existing nuclei to eliminate, (c) "move" action that chooses the location of one nucleus randomly from the existing nuclei to relocate. In step (3), we randomly chose one of the actions with equal probability. The unknowns are updated without the dimensional jump in the move action, while they are updated with the dimensional jump in the birth and death actions. We produced a new candidate of the unknowns for each action, and evaluated the candidates using the acceptance probability. The acceptance ratio is calculated

based on the formulation of Bodin and Sambridge [2009] and Galetti and Curtis [2018]. The details of the acceptance probability are written in Text S1.

In the birth action, we randomly chose a target fault-slip component from $J$ components. Then, we randomly added one nucleus for the target $j$th fault-slip component from the $K^{\mathrm{grid}}$ grid points except the currently existing nuclei listed in $\mathbf{c}_j$. According to this action, the total number of the nuclei for the $j$th fault-slip component was increased by 1 as $K_j' = K_j + 1$. Then, the locations of the nuclei were reformed as

$$\mathbf{c}'_j = \begin{pmatrix} \mathbf{c}_j \\ c'_{K_j'} \end{pmatrix} \tag{15}$$

where $c'_{K_j'}$ is the locational number of the new nucleus. The slips of the nuclei were also reformed as

$$\overline{\mathbf{s}}'_{k_j} = \begin{pmatrix} \overline{\mathbf{s}}_j \\ \overline{s}'_{K_j'} \end{pmatrix} \tag{16}$$

where the slip of the new cell $\overline{s}'_{K_j'}$ was derived from the slip of the existing cell where the new nucleus was introduced with perturbation. If the nucleus controlling the existing cell is defined as $k_j^{\mathrm{c}}$, the slip at the new cell $\overline{s}'_{K_j'}$can be written as

$$\overline{s}'_{K_j'} = \overline{s}_{k_j^{\mathrm{c}}} + v\sigma_{\mathrm{jump}} \tag{17}$$

where $\sigma_{\mathrm{jump}}$ is a constant denoting the standard deviation of the proposal PDF for the slip due to the dimensional jump.

In the death action, we randomly chose a target fault-slip component from $J$ components. Then, we randomly eliminated one nucleus of the target $j$th fault-slip component from the currently existing nuclei. According to this action, the total number of the nuclei for the $j$th fault-slip component was decreased by 1 as $K_j' = K_j - 1$. Then, the locations of the nuclei and the slips of the cells were reformed just excluding the corresponding fault-slip component.

In the move action, we randomly chose a target fault-slip component from $J$ components. Then, we randomly chose one nucleus from the currently existing nuclei of the target $j$th fault-slip component, and relocated its point to another nucleus randomly chosen from the grid points within specific distances from the original nucleus; the specific distances are defined by $r_{\mathrm{move}}^{\mathrm{str}}$ and $r_{\mathrm{move}}^{\mathrm{dip}}$ in the strike and dip directions, respectively. In this action, the total number of the

nuclei and the slips were kept $\mathbf{k}' = \mathbf{k}$ and $\overline{\mathbf{s}'} = \overline{\mathbf{s}}$. For the locations of the nuclei $\mathbf{c}_j'$, they were kept from the existing locations $\mathbf{c}_j$ except the chosen nucleus.

After these three steps, we sampled the unknowns with a specific loop interval of the loops if the number of the iteration loops $n$ was over the number of burn-in loops $N_{\text{burn-in}}$. To sample well-converged unknowns, the unknowns during the burn-in loops were discarded. As not all unknowns were updated in a single iteration loop, we only sampled the unknowns with a specific loop interval. In this study, we sampled every 100th iteration loop based on Bodin and Sambridge [2009]. Finally, we sampled the unknowns until $n$ reached $N_{\text{all}}$.

In this study, we performed the above rj-MCMC algorithm for $L$ multi-chains with (multi-chains approach); we assigned different initial values of $\mathbf{x}^{\text{ini}}$ for each chain and sampled the unknowns parallely from the multi-chains. As noted by Brooks et al. [2011] and Somogyvári and Reich [2019], the multi-chains approach is useful to reduce computational times by parallel computing compared with a long single-chain approach. Furthermore, calculating the ensemble of the samples from the multiple chains, we can obtain robust solutions regardless of influence on the initial values. As the length of each chain in the multi-chains approach is shorter than the long single-chain approach, the multi-chains approach is relatively sensitive to the length of the burn-in loops (i.e., degree of convergence). Thus, a parallel tempering technique has been often employed to accelerate the convergence [e.g., Sambridge, 2013; Dettmer et al., 2014]. However, this technique has difficulty in properly assigning the number of parallel replicas and their potential temperatures. Thus, we calculated solutions for the slip by a conventional ABIC-LSM, $\mathbf{s}^{\text{LSM}}$, and produced $L$ sets of the initial partitioned solutions $\overline{\mathbf{s}}^{\text{ini}}$ from $\mathbf{s}^{\text{LSM}}$ assuming various distributions of initial Voronoi nuclei ($\mathbf{c}^{\text{ini}}, \mathbf{k}^{\text{ini}}$). Because $\mathbf{s}^{\text{LSM}}$ can be regarded as well-converged initial values, we can perform the multi-chains approach effectively and simply without the parallel tempering technique. $\mathbf{s}^{\text{LSM}}$ was estimated following Yabuki and Matsu'ura [1992], and the details of this estimation method are written in Text S2.

In this study, we uniformly assigned the following configuration of rj-MCMC: $L = 2000$, $N_{\text{burn-in}} = 1000000$, $N_{\text{all}} = 1250000$, and $K_j^{\text{ini}} = 20$ $(j = 1, \cdots, J)$. Considering that the unknowns are sampled every 100th iteration loop, we fully obtained $5 \times 10^6$ samples from the multi-chains. Note that the initial distributions of the Voronoi nuclei $\mathbf{c}^{\text{ini}}$ were randomly generated from the nucleus grid following the number of the initial Voronoi nuclei $\mathbf{k}^{\text{ini}}$.

Moreover, we basically assigned the minimum and maximum numbers of the Voronoi nuclei for each fault-slip component as $K_j^{\min} = 5$ and $K_j^{\max} = 50$ $(j = 1, \cdots, J)$, respectively, which are used in Equation (S2) and (S3) of Text S1. We also assigned the minimum and maximum values of the weighting parameters as $\Lambda_i^{\min} = -10$ and $\Lambda_i^{\max} = 10$ $(i = 1, \cdots, I)$, respectively for the all estimations, which are used in Equation (S8) and (S9) of Text S1.

## 3 Synthetic tests

### 3.1 Model configuration

Here, we investigated performance of the trans-dimensional geodetic inversion using the rj-MCMC technique through synthetic tests assuming fault slips in a subduction zone. A plate interface with uniform dip of 15° in a semi-infinite space was assumed as shown in Figure S2. The fault domain was approximately 500 km (along strike) × 310 km (along dip), and its upper limit reached to the surface corresponding to the trench. We then laid sub-faults with size of approximately 20 km × 20.7 km on the plate interface, and total number of the sub-faults is 375. We located randomly distributed 150 synthetic observational sites within the a range of 200–400 km from the trench as onshore GNSS sites. Moreover, we located synthetic observational sites within the a range of 0–200 km from the trench as offshore GNSS-A sites. Three patterns of the offshore observational site distribution were assumed: (1) no site, (2) five randomly distributed sites, and (3) twenty-five randomly distributed sites. We calculated synthetic displacements at these sites due to a given fault slip distribution, and then we obtained synthetic observational data by adding observational errors.

### 3.2 Synthetic test 1: response to smooth coseismic slip

In the synthetic test, a smooth coseismic slip distribution with maximum slip of ~700 cm was provided to calculate synthetic observational data for three site patterns (“Target” column of Figure 2). In this test, we assumed an elastic media [Okada, 1992], and we calculated the Green functions in the directions of rake = 45° and of rake = 135° (i.e., the fault-slip components were

defined as $J = 2$, and total number of the unknowns for slip is $375 \times 2 = 750$). Then, imposing non-negative constraints on the slip, we restricted the slip rake within the range from 45° to 135° in the same manner as Miyazaki et al. [2011]. We assigned the minimum and maximum slips as $\overline{s}_j^{\min} = 0$ [cm] and $\overline{s}_j^{\max} = 3000$ [cm] $(j = 1,2)$, respectively. The observational errors were added as the Gaussian noises of

$$\left(\sigma_{\mathrm{on}_{\mathrm{hor}}}, \sigma_{\mathrm{on}_{\mathrm{ver}}}, \sigma_{\mathrm{off}_{\mathrm{hor}}}, \sigma_{\mathrm{off}_{\mathrm{ver}}}\right) = (1, 2, 3, 6)\ [\mathrm{cm}] \tag{18}$$

indicating standard deviations for horizontal components of the onshore sites, vertical component of the onshore sites, horizontal components of the offshore sites, and vertical component of the offshore sites, respectively. The standard deviations for the offshore sites are given following the case of the 2005 Miyagi-oki earthquake shown in Sato et al. [2013]. We provided single weighting parameter uniformly scaling all data for simplicity (i.e., $I = 1$). Because we assigned a diagonal matrix for the initial observational covariance matrix $\mathbf{E}_1^{\mathrm{ini}}$ following Equation (18), the weighting parameter should be zero (i.e., the weight matrix should be on the initial condition: $\mathbf{W}_1 = 10^0 \mathbf{W}_1^{\mathrm{ini}}$).

From the synthetic observational data, we estimated fault-slip distributions by the ABIC-LSM and the rj-MCMC method, which are shown in "ABIC-LSM" and "Rj-MCMC" columns of Figure 2, respectively. Note that the "Error" column of ABIC-LSM demonstrates standard deviations calculated from diagonal components of the covariance matrix. For the rj-MCMC results, we used two methods to express a slip distribution: mean and median of the samples. Moreover, we calculated the standard deviation of the samples ("SD" column) and the normalized interquartile range (NIQR) of samples ("NIQR" column) as estimation errors. The synthetic (without the observational errors), observational (with the observational errors), and calculated (from the estimated model) displacements are shown in Figure 2 as magenta, black, and blue vectors.

Figure 3c shows histograms of the unknowns for site pattern 2. The histograms demonstrated that total number of the unknowns for slip was reduced from 750 to ~10–12 by the Voronoi partition and that the weighting parameter was properly kept at zero. For the slip unknowns, the histograms at three sub-faults shown in Figure 3a are demonstrated for example. The slip at the $m$th sub-fault was calculated as $s_m = \sqrt{s_{m_1}^2 + s_{m_2}^2}$ when defining $s_{m_j}$ as the slip at the $m$th sub-fault in the $j$th fault-slip component. Figures S3 and S4 also show histograms for

the unknowns in the cases for site patterns 1 and 3, respectively. The histograms at the sub-fault A are similar to the Gaussian distribution in all cases of the site patterns, whereas we can find the histograms with multiple peaks or those with a biased distribution at the sub-fault B and at sub-fault C, respectively, in the cases of the site patterns 1–2. These histograms following non-Gaussian distributions are considered to be caused by the lack of the offshore observational sites as the slip amounts at these sub-fault were not well constrained. Although we showed the standard deviation of the samples to visualize estimation errors ("SD" in Figure 2), the standard deviation of the samples potentially assumes a Gaussian distribution of the samples. Thus, to visualize the estimation error following a non-Gaussian distribution, we also showed the map of NIQR. If the observational error follows a Gaussian distribution, NIQR corresponds to SD; therefore, we can roughly interpret that the estimation errors are close to Gaussian distributions when the mean and the standard deviation resemble the median and the median and the NIQR, respectively. Furthermore, to visualize details of the PDFs for the slip such as due to multiple peaks or a biased distribution, we calculated differences of the percentiles (subtracting 50th percentile from 5th, 25th, 75th, and 95th percentiles) in Figures 3b, S3b, and S4b. For example, we considered that a PDF of the slip amount shows a biased distribution with a long slope to the high slip; 5th and 25th percentile differences demonstrate small absolute values, while 75th and 95th percentile differences demonstrate large absolute values such as sub-fault C in the cases of the site patterns 1–2.

The target slip distributions were well reproduced both by the ABIC-LSM and by the rj-MCMC method for the cases of the site patterns 2 and 3. Furthermore, both of the ABIC-LSM and the rj-MCMC method underestimated the maximum slip for the case of the slip pattern 1 because no offshore site was employed. However, the estimated slip distribution of ABIC-LSM was obviously over-smoothed in the along-strike direction. By contrast, the rj-MCMC method reduced such over-smoothing in the along-strike direction. It is considered that this effect was caused by a sparse modeling behavior of the rj-MCMC method. Furthermore, among all site patterns, the rj-MCMC method successfully reduced spotting artificial slips appearing in the all slip distribution estimated by the ABIC-LSM. This effect is also considered to be provided as the sparse modeling behavior of the rj-MCMC method.

For all slip pattern cases, the slip distributions estimated by the rj-MCMC method generally show large slip near the trench compared with those estimated by the ABIC-LSM. This

362 is because the rj-MCMC method sampled a low probability of large slips near the trench as
363 demonstrated by the histograms of sub-fault C and the 95th percentile difference (Figures 3, S3,
364 and S4). Because spatial resolution near the trench was low due to the lack of the observational
365 sites, large coseismic slip there was considered to occur with low probability as modeled by the
366 rj-MCMC. However, ABIC-LSM cannot properly consider such a low probability phenomenon
367 in the solutions because Gaussian distribution of the solutions was assumed.

368 We showed two models for the results of the rj-MCMC method: the mean and median
369 models as shown in Figure 2. Their slip distributions were quite similar except the region near
370 the trench where the large slip was considered to occur with the low probability. Because the
371 median is generally smaller than the mean when the biased PDF with a long slope to the high slip
372 (e.g., the histogram of sub-fault C in Figure 3c), the seismic moment of the median model is
373 smaller than that of the mean model; for example, in the case of the site pattern 1, the moment
374 magnitude of the median model is $M_w$ 8.18, while that of the mean model is $M_w$ 8.24. We
375 evaluated the mean model as a better representative model because the seismic moments of the
376 mean model were generally close to the seismic moment of the target model. However, the
377 median model and its corresponding estimation error (NIQR) provided useful information to
378 know degree how the unknowns for the slip follow the Gaussian distribution or not as indicated
379 above.

380

381 3.3 Synthetic test 2: response to sharp coseismic slip

382 In this synthetic test, a sharp coseismic slip distribution with maximum slip of
383 approximately 1000 cm was provided to calculate synthetic observational data for the three site
384 patterns as in synthetic test 1, and then we estimated slip distributions by the ABIC-LSM and the
385 rj-MCMC method as shown in Figure 4. Considering the elasticity of plates, deformation due to
386 fault locking at asperities should be continuous; therefore, coseismic slip should be rather
387 continuous (i.e., edge of fault slip distribution tends to be smooth) [Herman et al., 2018]. Thus,
388 the target slip distribution in this synthetic test is slightly unrealistic but effective to evaluate the
389 performance of the inversion techniques.

390 The ABIC-LSM model failed to reproduce the target slip distribution in any cases of the
391 site patterns (Figure 4), because the assumption of the smoothing was unsuitable to model such a

sharp distribution. To forcibly reproduce sharp edges of the slip patch, the ABIC-LSM provided a weak smoothing constraint; hence, the estimated slip distributions were highly dependent on location of the observational sites especially as shown in site pattern 3. In contrast, the rj-MCMC method successfully reproduced the target slip distribution, because the Voronoi partition was potentially suitable for producing sharp edges. Summarising the results of the synthetic tests 1 and 2, the rj-MCMC method can flexibly represent a fault slip distribution regardless of the site distribution and of roughness on the target slip distribution.

### 3.4 Synthetic test 3: behavior of the weighting parameters

In this synthetic test, performance of the weighting parameters was investigated by applying incorrect initial observational errors. We provided the smooth coseismic slip distribution for the target slip distribution as employed in synthetic test 1 and performed the rj-MCMC inversion under the same conditions as synthetic test 1 except the observational errors. Note that we performed the inversion only for the data assuming the site pattern 3. Here, dual weighting parameters were employed (i.e., $I = 2$): the weighting parameter for the onshore observational data ($i = 1$) and that for the offshore observational data ($i = 2$), regardless of distinction between the horizontal and vertical components. Then, two types of the observational error conditions were investigated; one assumed that the true observational errors, which were added to the synthetic observational data, were smaller than the initial observational errors (the smaller error case); and the other assumed the true observational errors were larger than the initial observational errors (the larger error case). In the former case, the true observational errors were added as the Gaussian noises of

$$\left(\sigma_{\mathrm{on_{hor}}}, \sigma_{\mathrm{on_{ver}}}, \sigma_{\mathrm{off_{hor}}}, \sigma_{\mathrm{off_{ver}}}\right) = (1, 2, 3, 6)\ [\mathrm{cm}], \tag{19}$$

like synthetic test 1, while the initial observational errors were given as

$$\left(\sigma^{\mathrm{ini}}_{\mathrm{on_{hor}}}, \sigma^{\mathrm{ini}}_{\mathrm{on_{ver}}}, \sigma^{\mathrm{ini}}_{\mathrm{off_{hor}}}, \sigma^{\mathrm{ini}}_{\mathrm{off_{ver}}}\right) = (1, 2, 30, 60)\ [\mathrm{cm}]. \tag{20}$$

In the later case, the true observational errors were added as the Gaussian noises of

$$\left(\sigma_{\mathrm{on_{hor}}}, \sigma_{\mathrm{on_{ver}}}, \sigma_{\mathrm{off_{hor}}}, \sigma_{\mathrm{off_{ver}}}\right) = (1, 2, 30, 60)\ [\mathrm{cm}] \tag{21}$$

while the initial observational errors were given as

$$\left(\sigma^{\mathrm{ini}}_{\mathrm{on_{hor}}}, \sigma^{\mathrm{ini}}_{\mathrm{on_{ver}}}, \sigma^{\mathrm{ini}}_{\mathrm{off_{hor}}}, \sigma^{\mathrm{ini}}_{\mathrm{off_{ver}}}\right) = (1, 2, 3, 6)\ [\mathrm{cm}]. \tag{22}$$

For comparison, we also estimated fault slip distributions by the rj-MCMC method assuming the single weighting parameter in the same manner as synthetic test 1.

The upper panels of Figure 5 show the results for the smaller error case. When assuming the single weighting parameter, the estimated slip distribution and its standard deviation are similar to those of the synthetic test 1 for the site pattern 1. This similarity suggested that the offshore observational data were almost ignored because of the employed large initial observational errors (Equation 20). When assuming the dual weighting parameters, the estimated slip distribution and its standard deviation are similar to those of synthetic test 1 for site pattern 3 (Figure 2). This suggests that the weighting parameter for the offshore observational data increased the weights of the offshore observational data. Actually, the observational errors adjusted by the weighting parameters were given as

$$\begin{aligned}&\left(\hat{\sigma}_{\mathrm{on_{hor}}}, \hat{\sigma}_{\mathrm{on_{ver}}}, \hat{\sigma}_{\mathrm{off_{hor}}}, \hat{\sigma}_{\mathrm{off_{ver}}}\right) \\ &= \left(10^{-\frac{\Lambda_1}{2}}\sigma^{\mathrm{ini}}_{\mathrm{on_{hor}}}, 10^{-\frac{\Lambda_1}{2}}\sigma^{\mathrm{ini}}_{\mathrm{on_{ver}}}, 10^{-\frac{\Lambda_2}{2}}\sigma^{\mathrm{ini}}_{\mathrm{off_{hor}}}, 10^{-\frac{\Lambda_2}{2}}\sigma^{\mathrm{ini}}_{\mathrm{off_{ver}}}\right) \\ &= (1.01, 2.03, 4.36, 8.72)\ [\mathrm{cm}].\end{aligned} \tag{23}$$

The weighting parameters used in Equation (23) were calculated as the mean values of the rj-MCMC samples. The histograms of the weighting parameters are shown in Figure S5. Because the adjusted observational errors for the offshore data were rather larger than the true observational errors (Equation 19), the estimated slip distribution was also smoother than that of the synthetic test 1 for site pattern 3.

The lower panels of Figure 5 show the results for the larger error case. When assuming the single weighting parameter, the estimated slip distribution was extremely rough. In this result, the offshore observational data were over-fitted because of the employed small initial observational errors (Equation 22). By contrast, when assuming the dual weighting parameters, the estimated slip distribution reproduced the target smooth distribution by degrading the weights of the offshore observational data by the weighting parameters. The observational errors adjusted by the mean weighting parameters were given as

$$\begin{aligned}&\left(\hat{\sigma}_{\mathrm{on_{hor}}}, \hat{\sigma}_{\mathrm{on_{ver}}}, \hat{\sigma}_{\mathrm{off_{hor}}}, \hat{\sigma}_{\mathrm{off_{ver}}}\right) \\ &= \left(10^{-\frac{\Lambda_1}{2}}\sigma^{\mathrm{ini}}_{\mathrm{on_{hor}}}, 10^{-\frac{\Lambda_1}{2}}\sigma^{\mathrm{ini}}_{\mathrm{on_{ver}}}, 10^{-\frac{\Lambda_2}{2}}\sigma^{\mathrm{ini}}_{\mathrm{off_{hor}}}, 10^{-\frac{\Lambda_2}{2}}\sigma^{\mathrm{ini}}_{\mathrm{off_{ver}}}\right)\end{aligned} \tag{24}$$

$$= (1.01, 2.03, 31.77, 63.54)\ [\mathrm{cm}].$$

which are well fitted to the true observational errors (Equation 21). The histograms of the weighting parameters are shown in Figure S6 as well as the histograms of the other unknowns.

From the above results, the weighting parameters properly adjusted the initial observational errors by the data-driven approach. Considering that the initial large observational errors provided a little smooth slip distribution even using the weighting parameter (the smaller error case), we would assign rather small initial observational errors and adjust them by the weighting parameters in a practical use of the rj-MCMC method as shown later in Section 4.

### 3.5 Synthetic test 4: coupling estimation

In this synthetic test, we provided synthetic negative fault slips assuming annual interseismic coupling (Figure 6). An elastic media [Okada, 1992] was assumed, and we calculated the Green functions in the direction of rake=90° alone (i.e., $J = 1$). The minimum and maximum slip rates were assigned as $\overline{s}_1^{\min} = -83.5\ [\mathrm{mm/yr}]$ and $\overline{s}_1^{\max} = 500\ [\mathrm{mm/yr}]$, respectively. The minimum slip rate was provided as a subducting rate in the off-Tohoku region, Japan. The observational errors were added as the Gaussian noises of

$$\left(\sigma_{\mathrm{GNSS_{hor}}}, \sigma_{\mathrm{GNSS_{ver}}}, \sigma_{\mathrm{GNSS\text{-}A_{hor}}}\right) = (1.5, 3, 5)\ [\mathrm{mm/yr}]. \quad (25)$$

We ignored the vertical component of the offshore sites because the GNSS-A measurement has too large observational errors to discuss small coupling conditions. The standard deviation for the horizontal components of the offshore sites was given following the case of interseismic displacement rates for the Nankai and Tohoku regions shown in Sato et al. [2013] and Yokota et al. [2016]. The initial observational errors were given following the true observational errors (Equation 25), and the single weighting parameter was given ($I = 1$). The aim of this test was to assess performance of the rj-MCMC method for the coupling estimation and for difficult inversion conditions compared with the coseismic slip cases: multiple peaks of fault slip ("Target" of Figure 6) and low signal-noise ratio.

Figure 6 shows the inversion results estimated by the ABIC-LSM and the rj-MCMC method for site patterns 1 and 3. In the both of the site patterns, the ABIC-LSM provided fairly smooth coupling distributions because the difficult inversion conditions required strong

smoothing constraints. The rj-MCMC method also provided smooth coupling distributions for site pattern 1 due to the low spatial resolution in the offshore area. However, down-dip limits of the coupling distribution estimated by the rj-MCMC method were substantially constrained compared with those estimated by the ABIC-LSM. This indicated that flexibility of the spatial partition by the rj-MCMC method enables smooth edge expression of the up-dip limits (due to low spatial resolution) and relatively sharp edge expression of the down-dip limits (due to relatively high spatial resolution). The rj-MCMC method obviously demonstrated better performance for site pattern 3; peaks of the coupling distribution in the northern and middle regions were clearly obtained. Thus, the rj-MCMC method has superior ability to avoid the over-smoothing compared with the ABIC-LSM. Meanwhile, the southern peak of the coupling could not be imaged even by the rj-MCMC method because of its narrow spatial extent and insufficient deployment of the offshore observational sites.

Figure 6 shows that distributions of the standard deviation are obviously different from that of NIQR in both of the site patterns. This suggests the observational errors did not generally follow Gaussian distributions. Figures S7 and S8 show percentile differences and histograms of the unknowns for cases of site patterns 1 and 3, respectively. Figure S7 clearly shows positive slip with low probability in the northern area near the trench, and also indicates low spatial resolution there. Figure S8 shows multiple histogram peaks, especially the histogram for the slip at sub-fault D (in the northern area near the trench). For the sub-fault D, we can interpret that both possibilities of strong coupling and zero coupling are considered at the same level taking into account the insufficient spatial resolution. Thus, the rj-MCMC method is useful to assess how risk of the coupling occurs at each sub-fault from the histogram or the percentile difference, which cannot be expressed by the conventional ABIC-LSM.

### 3.6 Synthetic test 5: viscoelastic inversion

In this synthetic test, we provided synthetic coseismic slip distribution (period 1) and postseismic slip distributions with three time windows (periods 2–4; the duration for each period was set as one year). We assumed a two-layered viscoelastic media [Fukahata & Matsu'ura, 2004] in the same manner as Tomita et al. [2020]: viscosity in the lower media of $1.5 \times 10^{19}$ Pa s, thickness of the upper media of 50 km, rigidities in the upper and lower media of 40 GPa and

67 GPa, densities in the upper and lower media of 2800 kg/m$^3$ and 3300 kg/m$^3$, and Poisson's ratios in the upper and lower media of 0.25 and 0.27, respectively. We then calculated the viscoelastic Green functions in the directions of rake=45° and rake=135° for the coseismic slip and in the direction of rake=90° alone for the postseismic slip (i.e., $J = 5$). The minimum and maximum slips for the coseismic period were assigned as $\overline{s}_j^{\min} = 0$ [cm] and $\overline{s}_j^{\max} = 6000$ [cm] ($j = 1,2$), respectively, and those for the postseismic period were assigned as $\overline{s}_j^{\min} = -8.35$ [cm] and $\overline{s}_j^{\max} = 500$ [cm] ($j = 3, \cdots, 5$), respectively. Based on the 2011 Tohoku-oki earthquake, we assumed that the offshore sites were installed in the postseismic period (here, the period 3). The observational errors for the coseismic period were added as the Gaussian noises of

$$\left(\sigma_{\mathrm{GNSS_{hor}}}, \sigma_{\mathrm{GNSS_{ver}}}\right) = (1, 2)\ [\mathrm{cm}]. \tag{26}$$

The observational errors for the postseismic period were added as the Gaussian noises of

$$\left(\sigma_{\mathrm{GNSS_{hor}}}, \sigma_{\mathrm{GNSS_{ver}}}, \sigma_{\mathrm{GNSS\text{-}A_{hor}}}, \sigma_{\mathrm{GNSS\text{-}A_{ver}}}\right) = (0.5, 1, 2, 4)\ [\mathrm{cm/yr}]. \tag{27}$$

The standard deviations of the offshore sites were given following the postseismic displacements after the 2011 Tohoku-oki earthquake shown in Watanabe et al. [2014], Tomita et al. [2017], and Yokota et al. [2018]. The initial observational errors were given following the true observational errors, and the four weighting parameters were given to individual time-window ($I = 4$). The aim of this test was to assess performance of the rj-MCMC method for estimation of spatiotemporal evolution of fault slip, which basically requires many hyper-parameters constraining both spatial space and temporal space [e.g., Yoshioka et al., 2015]. In this case, we individually deployed Voronoi nuclei for each time-window and estimated fault slip distributions considering viscoelastic responses without any external constraints. Although we can introduce temporal smoothing constraints in our rj-MCMC method, we did not use the constraints for simplicity.

For comparison and obtaining initial values, we also performed the ABIC-LSM as well as the rj-MCMC method. In the rj-MCMC method, we simultaneously estimated the co- and post-seismic slip distributions based on the following observation equation for the viscoelastic inversion approach derived from Tomita et al. [2020]:

$$\begin{pmatrix}\mathbf{d}_1\\ \mathbf{d}_2\\ \mathbf{d}_3\\ \mathbf{d}_4\end{pmatrix}=\begin{pmatrix}\mathbf{G}^{e}_{1,1} & \mathbf{G}^{e}_{1,2} & \mathbf{0} & \cdots & \mathbf{0}\\ \mathbf{G}^{v}_{2,1} & \mathbf{G}^{v}_{2,2} & \mathbf{G}^{e}_{2,3} & \ddots & \vdots\\ \mathbf{G}^{v}_{3,1} & \mathbf{G}^{v}_{3,2} & \mathbf{G}^{v}_{3,3} & \mathbf{G}^{e}_{3,4} & \mathbf{0}\\ \mathbf{G}^{v}_{4,1} & \mathbf{G}^{v}_{4,2} & \mathbf{G}^{v}_{4,3} & \mathbf{G}^{v}_{4,4} & \mathbf{G}^{e}_{4,5}\end{pmatrix}\begin{pmatrix}\mathbf{s}_1\\ \mathbf{s}_2\\ \mathbf{s}_3\\ \mathbf{s}_4\\ \mathbf{s}_5\end{pmatrix}+\begin{pmatrix}\mathbf{e}_1\\ \mathbf{e}_2\\ \mathbf{e}_3\\ \mathbf{e}_4\end{pmatrix}, \tag{28}$$

where $\mathbf{G}^{e}$ and $\mathbf{G}^{v}$ represent the elastic and viscous Green functions, respectively. However, in the ABIC-LSM, we estimated a fault slip distribution of each time-window step by step as similar with Lubis et al. [2013] to avoid difficulty in determining multiple hyper-parameters.

Figure 7 shows the target and the estimated slip distributions. The slip and error maps of the rj-MCMC method demonstrated mean and standard deviation of the samples, respectively. The rj-MCMC results well reproduced the target distributions as well as the results of the ABIC-LSM except the period 2 in which effective offshore observational sites were absent. Unlike the ABIC-LSM, the rj-MCMC method successfully reduced artificial negative postseismic slip. Although the smoothing constraint of the ABIC-LSM cannot prevent generation of spotting artificial slips, the rj-MCMC method can prevent it by unifying the sub-faults by the Voronoi partition. Thus, the rj-MCMC method is useful to model such spatiotemporal evolution of the fault slip without any constraints. Additionally, as with the other synthetic tests above, the estimation errors imaged precision of the solutions, which cannot be assessed by the ABIC-LSM. We also showed median model at percentile differences in Figure S9 to assess non-Gaussian errors.

### 3.7 Checkerboard resolution test

From the above synthetic tests, the estimation errors of the rj-MCMC method (standard deviation and NIQR) demonstrated good performance of imaging precision of the solutions for the fault slip; however, it is difficult to consider spatial resolution from the results. To evaluate spatial resolution, we conducted checkerboard resolution tests. As it is difficult to evaluate spatial resolution for the overall fault space by single checkerboard pattern, we conducted the checkerboard resolution test for various patterns in which checkerboard patches were slightly shifted (Figure S10). Here, we generated eighteen total checkerboard patterns. Note that observational noises, which were given to generate the synthetic observational data, followed the observational errors adjusted by the weighing parameter in the synthetic test 1. The upper limits

548 of the Voronoi nuclei are set as $K_j^{\max} = 50$ $(j = 1,2)$ in the checkerboard resolution tests. Figure
549 8a shows an example of the inversion result for a single checkerboard pattern. The results for all
550 checkerboard patterns are shown in Figure S10. For each checkerboard pattern, a patch with the
551 size of ~60 × 60 km$^2$ and with the slip of ~425 cm was provided. The patch size and the slip
552 amount for patch should be manually changed to comform with our target slip behavior by which
553 we intend to assess sensitivity of the observational data to. To summarize the results, we
554 introduced a new indicator called as the "reconstruction ratio". The reconstruction ratio for a
555 sub-fault $m$ is written as follows:

$$RR_m = 100 - \frac{1}{\tilde{L}} \frac{\sum_{l=1}^{L} \left| \tilde{s}_{m,l}^{\mathrm{cal}} - s_{m,l}^{\mathrm{syn}} \right|}{s^{\mathrm{syn}}} \times 100\ [\%], \tag{29}$$

556 $$\text{with} \quad \tilde{s}_{m,l}^{\mathrm{cal}} = \begin{cases} s_{m,l}^{\mathrm{cal}} & if \ \ s_{m,l}^{\mathrm{syn}} > 0 \\ 0 & if \ \ s_{m,l}^{\mathrm{syn}} = 0 \end{cases},$$

557 where $s^{\mathrm{syn}}$ is the slip amount of the slip patch (~425 cm in this case), and $s_{m,l}^{\mathrm{cal}}$ and $s_{m,l}^{\mathrm{cal}}$ are the
558 estimated and the target slips at the sub-fault $m$ for the pattern $l$, respectively. Moreover, $L$ is the
559 total number of the checkerboard patterns ($L = 18$), and $\tilde{L}$ is the total number of the
560 checkerboard pattern that provided the slip (non-zero slip) at the sub-fault $m$. As defined by $\tilde{s}_{m,l}^{\mathrm{cal}}$,
561 we only considered recovery at the sub-faults where synthetic slip was provided by the target slip
562 distribution. Because we provided a set of normal and reverse checkerboard patterns (see the
563 target distributions of 1 and 4 in Figure S10, for example), $\tilde{L} = L/2$. A map of the reconstruction
564 ratio (Figure 8b) clearly demonstrated that high reconstruction ratios (corresponding to high
565 spatial resolution) appeared roughly below the observational sites. A checkerboard resolution test
566 has been often performed in ABIC-LSM aproaches; however, it is difficult to assess intrinsic
567 sensitivity of the observational data because the degree of recovery was quite influenced by
568 strength of a smoothing constraint in ABIC-LSMs. If the smoothing constraint is optimized for a
569 checkerboard slip distribution, it is not suitable for a practical slip distribution. Whereas, if the
570 smoothing constraint is optimized for a practical slip distribution, it is not suitable for a
571 checkerboard slip distribution. Meanwhile, as the smoothing constraint is not used in the rj-
572 MCMC method, the checkerboard resolution tests through the rj-MCMC method are much
573 effective to demonstrate sensitivity of the observational data.

## 4 Application to the 2011 Tohoku-oki earthquake

Here, we applied the rj-MCMC method to coseismic geodetic observational data associated with the 2011 Tohoku-oki earthquake (March 11, 2011). We constructed 485 sub-faults based on the plate interface model of Iwasaki et al. [2015]. As with synthetic test 1, an elastic media [Okada, 1992] was assumed, and the Green functions in the directions of rake=45° and of rake=135° were calculated ($J = 2$; total number of the unknowns for slip is $485 \times 2 = 970$). When calculating the Green functions for offshore sites (denoted later), we considered seafloor depths by biasing the depths of the sub-faults along the plate interface in the same manner as Iinuma et al. [2012]. Minimum and maximum slips were assigned as $\overline{s_j}^{\min} = 0$[m] and $\overline{s_j}^{\max} = 100$ [m] ($j = 1,2$), respectively.

We employed the following types of the observational data: onshore GNSS (horizontal and vertical), offshore GNSS-A (horizontal and vertical), and offshore OBP gauge (vertical) data. The onshore GNSS data were differences between the daily coordinate solutions for the day before the mainshock (March 10, 2011) and those for the day after the mainshock (March 12, 2011) at 370 GNSS sites maintained by the Geospatial Information Authority of Japan (GSI) and Tohoku University, which were obtained by Tomita et al. [2020]. The offshore GNSS-A data were provided by the Japan Coast Guard (six sites with horizontal and vertical components) [Sato et al., 2011; Yokota et al., 2018] and Tohoku University (two sites with horizontal component only) [Kido et al., 2011]. The offshore OBP data were provided by University of Tokyo and Tohoku University (six sites) [Ito et al. 2011; Meade et al., 2011] as summarized by Iinuma et al. [2012]. The onshore GNSS and the offshore OBP data indicate almost pure coseismic displacements, while the offshore GNSS-A data include not only coseismic displacements but also early (~1 month) postseismic displacements [Kido et al., 2011; Sato et al., 2011]. Then, as for the offshore GNSS-A data, it is unsuitable to assign instrumental measurement errors as observational errors for the inversion analysis considering the observational errors included not only instrumental measurement errors but also the modeling errors of the early postseismic displacements. Thus, we adopted an approach providing rough initial observational errors of the offshore GNSS-A data and then adjusting them by the weighting parameters. The observational errors of the offshore GNSS-A data in the horizontal

and vertical components were quite different for both the instrumental measurement errors and the early postseismic displacements; hence, we provided three weighting parameters ($I = 3$) for the horizontal GNSS-A data, vertical GNSS-A data, and other data. The initial observational errors were given as follows:

$$\left(\sigma^{\mathrm{ini}}_{\mathrm{GNSS_{hor}}}, \sigma^{\mathrm{ini}}_{\mathrm{GNSS_{ver}}}, \sigma^{\mathrm{ini}}_{\mathrm{OBP_1}}, \sigma^{\mathrm{ini}}_{\mathrm{OBP_2}}, \sigma^{\mathrm{ini}}_{\mathrm{GNSS\text{-}A_{hor}}}, \sigma^{\mathrm{ini}}_{\mathrm{GNSS\text{-}A_{ver}}}\right) = (2.5, 5, 10, 2.5, 20, 20)\ [\mathrm{cm}]. \tag{30}$$

The onshore GNSS data potentially had standard deviations of a few centimeter as the observational errors from the previous geodetic slip inversion studies [Iinuma et al., 2012; Tomita et al., 2020]. The observational errors for $OBP_1$ [Maeda et al., 2011] and $OBP_2$ [Ito et al., 2011] were roughly given from measurement errors following Iinuma et al. [2012]. We provided relatively small observational errors for the GNSS-A data compared with the instrumental measurement errors (from several tens of centimeters [Sato et al. 2011] to ~1 meter [Kido et al., 2011]). We then assigned the initial observational covariance matrices $\mathbf{E}_i^{\mathrm{ini}} (i = 1, \cdots, 3)$ following Equation (30). Meanwhile, as for the ABIC-LSM, a diagonal observational covariance matrix was given based on the following relative observational errors:

$$\sigma_{\mathrm{GNSS_{hor}}} : \sigma_{\mathrm{GNSS_{ver}}} : \sigma_{\mathrm{OBP_1}} : \sigma_{\mathrm{OBP_2}} : \sigma_{\mathrm{GNSS\text{-}A_{hor}}} : \sigma_{\mathrm{GNSS\text{-}A_{ver}}} = 1 : 2 : 2 : 1 : 10 : 10. \tag{31}$$

Because the ABIC-LSM tends to generate larger misfits in the offshore area for the case of the 2011 Tohoku-oki earthquake, we determined the relative observational errors by trial and error.

Figure 9 shows the estimated slip distributions and the estimation errors, and Figure 10 shows percentile differences and histograms for the unknowns. Through the rj-MCMC method, the weighting parameters were determined as Figure 10c. Using the estimated weighting parameters (mean values of samples), the adjusted observational errors are obtained as follows:

$$\begin{aligned}&\left(\sigma_{\mathrm{GNSS_{hor}}}, \sigma_{\mathrm{GNSS_{ver}}}, \sigma_{\mathrm{OBP_1}}, \sigma_{\mathrm{OBP_2}}, \sigma_{\mathrm{GNSS\text{-}A_{hor}}}, \sigma_{\mathrm{GNSS\text{-}A_{ver}}}\right) \\ &= \left(10^{-\frac{\Lambda_1}{2}}\sigma^{\mathrm{ini}}_{\mathrm{GNSS_{hor}}}, 10^{-\frac{\Lambda_1}{2}}\sigma^{\mathrm{ini}}_{\mathrm{GNSS_{ver}}}, 10^{-\frac{\Lambda_1}{2}}\sigma^{\mathrm{ini}}_{\mathrm{OBP_1}}, 10^{-\frac{\Lambda_1}{2}}\sigma^{\mathrm{ini}}_{\mathrm{OBP_2}}, 10^{-\frac{\Lambda_2}{2}}\sigma^{\mathrm{ini}}_{\mathrm{GNSS\text{-}A_{hor}}}, 10^{-\frac{\Lambda_3}{2}}\sigma^{\mathrm{ini}}_{\mathrm{GNSS\text{-}A_{ver}}}\right) \\ &= (2.47, 4.93, 9.86, 2.47, 177.32, 59.20)\ [\mathrm{cm}].\end{aligned} \tag{32}$$

The adjusted observational errors for the GNSS and OBP data did not significantly changed from the initial values, while those for the GNSS-A data indicated large uncertainties. Considering the instrumental measurement errors (from several tens of centimeters [Sato et al., 2011] to ~1 meter [Kido et al., 2011]) and the early postseismic displacements (especially affecting the horizontal components), the adjusted large observational errors for the GNSS-A data are reasonable.

628 Furthermore, histograms of the weighting parameters for the GNSS-A data show wide ranges
629 (Figure 10). This is because the total number of the GNSS-A data is small. Although previous
630 ABIC-LSM studies have often considered relative weights between different observational data
631 [e.g., Funning et al., 2014], the relative weights were finally fixed to certain values optimized by
632 the ABIC criterion. By contrast, the rj-MCMC method can obtain slip distributions considering
633 wide ranges of the weighting parameter through the MCMC sampling process.
634 Figure 9 shows that the slip distributions estimated by the rj-MCMC method were similar
635 to the slip distribution estimated by the ABIC-LSM, which show large coseismic slip over 20 m
636 at the up-dip portion of the plate interface in the off-Miyagi region (the central portion of the
637 fault zone, called as the main rupture area) and small coseismic slip less than 20 m at the down-
638 dip portion of the plate interface in the off-Fukushima region (the southern portion of the fault
639 zone, called as the sub-rupture area). These features are the same as previous studies [e.g., Yagi
640 & Fukahata, 2011; Iinuma et al., 2012; Ozawa et al., 2012; Yue & Lay, 2013].
641 Comparing the results of the ABIC-LSM and the rj-MCMC method, the rj-MCMC
642 method provided relatively large slip near the trench (Figure 9). This feature was the same as the
643 results of the synthetic tests (e.g., Figure 2). The estimation error maps (SD and NIQR) of the rj-
644 MCMC method demonstrate small errors just below the offshore observational sites and large
645 errors in the northern and southern portions of the main rupture area (especially, around 38.5°N
646 near the trench and around 37.5°N). These large estimation errors were caused by low spatial
647 resolution due to lack of offshore observational sites. We can find the low spatial resolution there
648 by checkerboard resolution tests (Figure 11a; Figure S11) and reconstruction ratio (Figure 11b).
649 In the checkerboard resolution tests, each slip patch has the slip amount of ~21.2 m, and size of
650 the slip patch is ~80 × 80 $km^2$. Moreover, Figure 10b and 10c demonstrate that large coseismic
651 slip with low probability was obtained in the areas with the large estimation errors as clearly seen
652 by difference between the 95th and 50th percentiles and by a histogram for the slip at sub-fault
653 C; i.e., the slip amount there was basically estimated to be zero, but it might be large in low
654 probability. Such high coseismic slip with low probability cannot be investigated by the
655 conventional ABIC-LSM because of its assumption that the estimation errors follow a Gaussian
656 distribution. Meanwhile, we can also find low spatial resolution in the sub-rupture area (Figure
657 11b). However, unlike the large estimation error areas around the main rupture area, quite large
658 coseismic slip did not be sampled (Figure 10b and Figure 10c for the sub-fault A). Thus, we

659 figured out that the sub-rupture did not reach high slip amount such as the main rupture, but
660 spatial extent of the sub-rupture might not be well constrained considering the low spatial
661 resolution.

662

663 **5 Summary**

664 In this study, we developed the trans-dimensional geodetic inversion approach using the
665 rj-MCMC method based on the Voronoi partition and assessed its performance by the five
666 synthetic tests and the application to the 2011 Tohoku-oki earthquake.

667 Throughout the synthetic tests and the application, the rj-MCMC method demonstrated
668 similar or superior performance compared with the conventional ABIC-LSM from the point of
669 view of reproducing fault slip distributions. Because of the absence of the smoothing constraints,
670 the rj-MCMC method can flexibly express fault slip distributions; both of the smooth and the
671 sharp fault slip distributions can be reproduced (e.g., synthetic tests 1 and 2), and the spatially
672 non-uniform degree of the fault slip smoothness can be expressed (e.g., site pattern 1 in synthetic
673 tests 1 and 4, showing the sharp down-dip limits of slip and the smooth up-dip slip limits of slip).
674 Especially in synthetic test 4, non-uniformness of the fault slip distributions reflected spatial
675 heterogeneity of the data sensitivity to fault slips depending on spatial coverage of observational
676 sites. Because geodetic observational data often have large variation of their spatial coverage as
677 shown in the application of the 2011 Tohoku earthquake, the rj-MCMC method is suitable to
678 handle such geodetic observational data for appropriately imaging a fault slip distrition following
679 the data sensitivity. Moreover, the rj-MCMC method can prevent the occurrence of the artificial
680 spotting slips that cannot be avoided by the conventional ABIC-LSM. This benefit is provided
681 due to sparsity of number of unknowns introduced by the Voronoi partition.

682 One of utilities of the MCMC sampling is in obtaining the estimation errors following a
683 non-Gaussian distribution. As shown in the synthetic tests and application (especially, synthetic
684 test 4 and application), we successfully obtained slip parameters following non-Gaussian
685 distributions, which cannot be expressed by the conventional ABIC-LSM. These non-Gaussian
686 estimation errors suggested further detailed information on fault slip behavior such as high
687 coseismic rupture or strong fault locking in regions with low spatial resolution, which are useful
688 for coupling risk assessment or evaluation of large co- and post-seismic fault slip events.

Meanwhile, we demonstrated utility of the percentile differences (e.g., Figures 3b, S4b, S5b and 10b) to roughly understand distributions of the estimation errors in map views.

For the conventional ABIC-LSM, the estimation error and spatial resolution are affected by the prior information, such as the spatially uniform smoothing constraint; thus, they uniformly vary depending on strength of the smoothing constraint. Although the rj-MCMC method also have influence on the prior information, such as the Voronoi-partition assumption, we can easily evaluate precision of the unknowns from standard deviation, NIQR, or PDF histograms of the MCMC samples without such spatial uniform dependency. Meanwhile, it is difficult to assess spatial resolution (i.e., sensitivity of the observational data to fault slips) from a series of the samples obtained by performing the rj-MCMC method once. To assess this, it is effective to conduct the checkerboard resolution tests (Sections 3.7 and 4). We also introduced an indicator of the reconstruction ratio averaging various patterns of the checkerboard resolution tests and demonstrated its usefulness in considering the spatial resolution.

Our results also showed utility of the weighting (hierarchical scaling) parameters implemented in the MCMC sampling. As shown in synthetic test 3, the weighting parameters can appropriately adjust the initial observational errors to the given observational errors. The adjustment of the observational errors provided us reasonable fault slip distributions. Moreover, as the weighing parameters were sampled through the MCMC procedure as well as the other unknowns, we can obtain the estimated slip distributions considering the possible extents of the weighting parameters as shown in the weighting parameter histograms (e.g., Figures 3c, S4c, S5c, and 10c). This is one of advantage of the MCMC method compared with ABIC-LSMs that can adjust relative weighting parameters but cannot consider their possible extents. Furthermore, we can easily handling multiple weighting parameters. These flexibilities of the weighting parameters are quite useful for modeling geodetic data that included various kinds of measurements as shown in the application to the 2011 Tohoku earthquake.

As indicated above, the developed rj-MCMC method has various advantages compared with the conventional ABIC-LSMs; therefore, we conclude that it is effective for inverting geodetic observational data into fault slips. The rj-MCMC method can be widely used for estimating coseismic slip distributions, postseismic slip distributions considering viscoelastic Green’s functions, coupling distributions, and it is useful to assess the detailed fault slip

719 behaviors even if the slip parameters follow non-Gaussian distributions and spatially non-
720 uniform roughness.

721

722 **Acknowledgments, Samples, and Data**

723 The plate models by Iwasaki et al. [2015] were constructed from topography and bathymetry
724 data by Geospatial Information Authority of Japan (250-m digital map), Japan Oceanographic
725 Data Center (500 m mesh bathymetry data, J-EGG500,
726 http://www.jodc.go.jp/jodcweb/JDOSS/infoJEGG_j.html), and Geographic Information Network
727 of Alaska, University of Alaska [Lindquist et al., 2004]. The figures were generated using
728 Generic Mapping Tools software [Wessel and Smith, 1998]. This research was supported by
729 Japan Society for the Promotion of Science (JSPS) KAKENHI (Grant Number: 20K14588).
730

731 **References**

732 Amey, R. M. J., Hooper, A., & Morishita, Y. (2019), Going to Any Lengths: Solving for Fault
733 Size and Fractal Slip for the 2016, Mw 6.2 Central Tottori Earthquake, Japan, Using a
734 Transdimensional Inversion Scheme. *Journal of Geophysical Research: Solid Earth*,
735 124(4), 4001–4016. doi:10.1029/2018JB016434
736 Amey, R. M. J., Hooper, A., & Walters, R. J. (2018), A Bayesian Method for Incorporating Self-
737 Similarity Into Earthquake Slip Inversions. *Journal of Geophysical Research: Solid Earth*,
738 123(7), 6052–6071. doi:10.1029/2017JB015316
739 Bayes, T (1763) An essay towards solving a problem in the doctrine of chances. Philos Trans R
740 Soc Lond A, 53:370–418
741 Bodin, T., & Sambridge, M. (2009), Seismic tomography with the reversible jump algorithm.
742 *Geophysical Journal International*, 178(3), 1411–1436. doi:10.1111/j.1365-
743 246X.2009.04226.x
744 Bodin, T., Sambridge, M., Gallagher, K., & Rawlinson, N. (2012), Transdimensional inversion
745 of receiver functions and surface wave dispersion. *Journal of Geophysical Research: Solid*
746 *Earth*, 117(B2). doi:10.1029/2011JB008560

747 Brooks, S., Gelman, A., Jones. G., & Meng. X. L. (2011), Handbook of Markov chain Monte
748 Carlo. *Chapman & Hall/CRC*, New York.
749 Dettmer, J., Benavente, R., Cummins, P. R., & Sambridge, M. (2014), Trans-dimensional finite-
750 fault inversion. *Geophysical Journal International*, 199(2), 735–751.
751 doi:10.1093/gji/ggu280
752 Dettmer, J., Hawkins, R., Cummins, P. R., Hossen, J., Sambridge, M., Hino, R., & Inazu, D.
753 (2016), Tsunami source uncertainty estimation : The 2011 Japan tsunami. *Journal of*
754 *Geophysical Research: Solid Earth*, 121, 4483–4505. doi: 10.1002/2015JB012764.
755 Du, Y., Aydin, A., & Segall, P. (1992), Comparison of various inversion techniques as applied to
756 the determination of a geophysical deformation model for the 1983 Borah Peak earthquake.
757 *Bulletin of the Seismological Society of America*, 82(4), 1840–1866.
758 Evans, E. L., & Meade, B. J. (2012), Geodetic imaging of coseismic slip and postseismic
759 afterslip: Sparsity promoting methods applied to the great Tohoku earthquake. *Geophysical*
760 *Research Letters*, 39(11), 1–7. doi:10.1029/2012GL051990
761 Fukuda, J., & Johnson, K. M. (2008), A fully Bayesian inversion for spatial distribution of fault
762 slip with objective smoothing. *Bulletin of the Seismological Society of America*, 98(3),
763 1128–1146. doi:10.1785/0120070194
764 Funning, G. J., Fukahata, Y., Yagi, Y., & Parsons, B. (2014), A method for the joint inversion of
765 geodetic and seismic waveform data using ABIC : application to the 1997 Manyi, Tibet,
766 earthquake. *Geophysical Journal International*, 196, 1564–1579. doi:10.1093/gji/ggt406
767 Galetti, E., & Curtis, A. (2018), Transdimensional Electrical Resistivity Tomography. *Journal of*
768 *Geophysical Research: Solid Earth*, 123(8), 6347–6377. doi:10.1029/2017JB015418
769 Green, P. J. (1995), Reversible jump Markov chain Monte Carlo computation and Bayesian
770 model determination. *Biometrika*, 82(4), 711–732. doi:10.1093/biomet/82.4.711
771 Hallo, M., & Gallovič, F. (2020), Bayesian Self-Adapting Fault Slip Inversion With Green's
772 Functions Uncertainty and Application on the 2016 Mw7.1 Kumamoto Earthquake.
773 *Journal of Geophysical Research: Solid Earth*, 125(3), e2019JB018703.
774 doi:10.1029/2019JB018703
775 Hastings, W. K. (1970), Monte Carlo sampling methods using Markov chains and their
776 applications, *Biometrika*, 57, 97- 109, doi:10.2307/2334940.

777 Hawkins, R., Bodin, T., Sambridge, M., Choblet, G., & Husson, L. (2019), Trans-Dimensional
778 Surface Reconstruction With Different Classes of Parameterization. *Geochemistry,*
779 *Geophysics, Geosystem*s, 20(1), 505–529. doi:10.1029/2018GC008022
780 Hawkins, R., & Sambridge, M. (2015), Geophysical imaging using trans-dimensional trees.
781 *Geophysical Journal International*, 203, 972–1000. doi:10.1093/gji/ggv326
782 Herman, M. W., Furlong, K. P., & Govers, R. (2018), The Accumulation of Slip Deficit in
783 Subduction Zones in the Absence of Mechanical Coupling: Implications for the Behavior
784 of Megathrust Earthquakes. *Journal of Geophysical Research: Solid Earth*, 123(9), 8260–
785 8278. doi:10.1029/2018JB016336
786 Hori, M. (2001), Inverse analysis method using spectral decomposition of Green's function.
787 *Geophysical Journal International*, 147(1), 77–87. doi:10.1111/j.1365-246X.2001.00505.x
788 Iinuma, T., Hino, R., Kido, M., Inazu, D., Osada, Y., Ito, Y., Ohzono, M., Tsushima, H., Suzuki,
789 S., Fujimoto, H., & Miura, S. (2012), Coseismic slip distribution of the 2011 off the Pacific
790 Coast of Tohoku Earthquake (M9.0) refined by means of seafloor geodetic data. *Journal of*
791 *Geophysical Research: Solid Earth*, 117, B07409. doi:10.1029/2012JB009186
792 Ito, Y., Tsuji, T., Osada, Y., Kido, M., Inazu, D., Hayashi, Y., Tsushima, H., Hino, R., &
793 Fujimoto, H. (2011), Frontal wedge deformation near the source region of the 2011
794 Tohoku-Oki earthquake. *Geophysical Research Letters*, 38, L00G05.
795 doi:10.1029/2011GL048355
796 Iwasaki, T., Sato, H., Shinohara, M., Ishiyama, T. & Hashima, A. (2015), Fundamental structure
797 model of island arcs and subducted plates in and around Japan, *2015 Fall Meeting,*
798 *American Geophysical Union*, San Francisco, Dec. 14-18, T31B-2878.
799 Kido, M., Osada, Y., Fujimoto, H., Hino, R., & Ito, Y. (2011), Trench-normal variation in
800 observed seafloor displacements associated with the 2011 Tohoku-Oki earthquake.
801 *Geophysical Research Letters*, 38, L24303. doi:10.1029/2011GL050057
802 Kimura, H., Tadokoro, K., & Ito, T. (2019), Interplate Coupling Distribution Along the Nankai
803 Trough in Southwest Japan Estimated From the Block Motion Model Based on Onshore
804 GNSS and Seafloor GNSS/A Observations. *Journal of Geophysical Research: Solid Earth*,
805 124(6), 6140–6164. doi:10.1029/2018JB016159

806 Kubo, H., Asano, K., Iwata, T., & Aoi, S. (2016), Development of fully Bayesian multiple-time-
807 window source inversion. *Geophysical Journal International*, 204(3), 1601–1619.
808 doi:10.1093/gji/ggv540
809 Lindquist, K. G., K. Engle, D. Stahlke, and E. Price (2004), Global Topography and Bathymetry
810 Grid Improves Research Efforts, Eos Trans. AGU, 85(19), 186.
811 Lubis, A. M., Hashima, A., & Sato, T. (2013), Analysis of afterslip distribution following the
812 2007 September 12 southern Sumatra earthquake using poroelastic and viscoelastic media.
813 *Geophysical Journal International*, 192(1), 18–37. doi:10.1093/gji/ggs020
814 Maeda, T., Furumura, T., Sakai, S., & Shinohara, M. (2011), Significant tsunami observed at
815 ocean-bottom pressure gauges during the 2011 off the Pacific coast of Tohoku Earthquake.
816 *Earth, Planets and Space*, 63(7), 803–808. doi:10.5047/eps.2011.06.005
817 Metropolis, N., Rosenbluth, A. W., Rosenbluth, M. N., Teller, A. H., & Teller, E. (1953),
818 Equations of state calculations by fast computing machines, *Journal of Chemical Physics*,
819 21, 1087-1092.
820 Minson, S. E., Simons, M., & Beck, J. L. (2013), Bayesian inversion for finite fault earthquake
821 source models I—theory and algorithm. *Geophysical Journal International*, 194, 1701–
822 1726. doi:10.1093/gji/ggt180
823 Miyazaki, S., McGuire, J. J., & Segall, P. (2011), Seismic and aseismic fault slip before and
824 during the 2011 off the Pacific coast of Tohoku Earthquake. *Earth, Planets and Space*, 63,
825 637–642. doi:10.5047/eps.2011.07.001
826 Okada, Y. (1992), Internal deformation due to shear and tensile faults in a half-space, *Bulletin of*
827 *the Seismological Society of America*, 82, 1018–1040.
828 Ozawa, S., Nishimura, T., Munekane, H., Suito, H., Kobayashi, T., Tobita, M., & Imakiire, T.
829 (2012), Preceding, coseismic, and postseismic slips of the 2011 Tohoku earthquake, Japan.
830 *Journal of Geophysical Research: Solid Earth*, 117, B07404. doi: 10.1029/2011JB009120
831 Jin, H., Kato, T., & Hori, M. (2007), Estimation of slip distribution using an inverse method
832 based on spectral decomposition of Green ’s function utilizing Global Positioning System
833 (GPS) data. *Journal of Geophysical Research*, 112, B07414. doi: 10.1029/2004JB003378
834 Sambridge, M. (2013), A Parallel Tempering algorithm for probabilistic sampling and
835 multimodal optimization. *Geophysical Journal International*, 196(1), 357–374.
836 doi:10.1093/gji/ggt342

837 Sambridge, M., Gallagher, K., Jackson, A., & Rickwood, P. (2006), Trans-dimensional inverse
838 problems, model comparison and the evidence. *Geophysical Journal International*, 167(2),
839 528–542. doi:10.1111/j.1365-246X.2006.03155.x
840 Sato, M., Fujita, M., Matsumoto, Y., Ishikawa, T., Saito, H., Mochizuki, M., & Asada, A.
841 (2013), Interplate coupling off northeastern Japan before the 2011 Tohoku-oki earthquake,
842 inferred from seafloor geodetic data. *Journal of Geophysical Research: Solid Earth*,
843 118(7), 3860–3869. doi:10.1002/jgrb.50275
844 Sato, M., Ishikawa, T., Ujihara, N., Yoshida, S., Fujita, M., Mochizuki, M., & Asada, A. (2011).
845 Displacement Above the Hypocenter of the 2011 Tohoku-Oki Earthquake. *Science*,
846 332(6036), 1395. doi:10.1126/science.1207401
847 Somogyvári, M., & Reich, S. (2019), Convergence Tests for Transdimensional Markov Chains
848 in Geoscience Imaging. *Mathematical Geosciences*. doi:10.1007/s11004-019-09811-x
849 Tomita, F., Iinuma, T., Ohta, Y., Hino, R., Kido, M., & Uchida, N. (2020), Improvement on
850 spatial resolution of a coseismic slip distribution using postseismic geodetic data through a
851 viscoelastic inversion. *Earth, Planets and Space*, 72(1), 84. doi:10.1186/s40623-020-
852 01207-0
853 Tomita, F., Kido, M., Ohta, Y., Iinuma, T., & Hino, R. (2017), Along-trench variation in seafloor
854 displacements after the 2011 Tohoku earthquake. *Science Advances*, 3, e1700113.
855 doi:10.1126/sciadv.1700113
856 Watanabe, S. ichi, Sato, M., Fujita, M., Ishikawa, T., Yokota, Y., Ujihara, N., & Asada, A.
857 (2014), Evidence of viscoelastic deformation following the 2011 Tohoku-Oki earthquake
858 revealed from seafloor geodetic observation. *Geophysical Research Letters*, 41, 5789–
859 5796. doi:10.1002/2014GL061134
860 Wessel, P., & Smith, W. H. F. (1998), New, improved version of the Generic Mapping Tools
861 released. *Eos Trans AGU*, 79(47):579
862 Xu, X., Sandwell, D. T., & Bassett, D. (2018), A spectral expansion approach for geodetic slip
863 inversion: implications for the downdip rupture limits of oceanic and continental
864 megathrust earthquakes. *Geophysical Journal International*, 212(1), 400–411.
865 doi:10.1093/gji/ggx408

Yabuki, T., & Matsu'ura, M. (1992), Geodetic data inversion using a Bayesian information criterion for spatial distribution of fault slip. *Geophysical Journal International*, 109(2), 363–375. doi:10.1111/j.1365-246X.1992.tb00102.x

Yagi, Y., & Fukahata, Y. (2011), Rupture process of the 2011 Tohoku-oki earthquake and absolute elastic strain release. *Geophysical Research Letters*, 38(19), 1–5. doi:10.1029/2011GL048701

Yokota, Y., Ishikawa, T., & Watanabe, S. (2018), Seafloor crustal deformation data along the subduction zones around Japan obtained by GNSS-A observations. *Scientific Data*, 5, 180182. doi:10.1038/sdata.2018.182

Yokota, Y., Ishikawa, T., Watanabe, S., Tashiro, T., & Asada, A. (2016), Seafloor geodetic constraints on interplate coupling of the Nankai Trough megathrust zone. *Nature*, 534, 374–377. doi:10.1038/nature17632

Yoshioka, S., Matsuoka, Y., & Ide, S. (2015), Spatiotemporal slip distributions of three long-term slow slip events beneath the Bungo Channel, southwest Japan, inferred from inversion analyses of GPS data. *Geophysical Journal International*, 201(3), 1437–1455. doi:10.1093/gji/ggv022

Yue, H., & Lay, T. (2013), Source Rupture Models for the Mw 9.0 2011 Tohoku Earthquake from Joint Inversions of High-Rate Geodetic and Seismic Data. *Bulletin of the Seismological Society of America*, 103(2), 1242–1255. doi:10.1785/0120120119

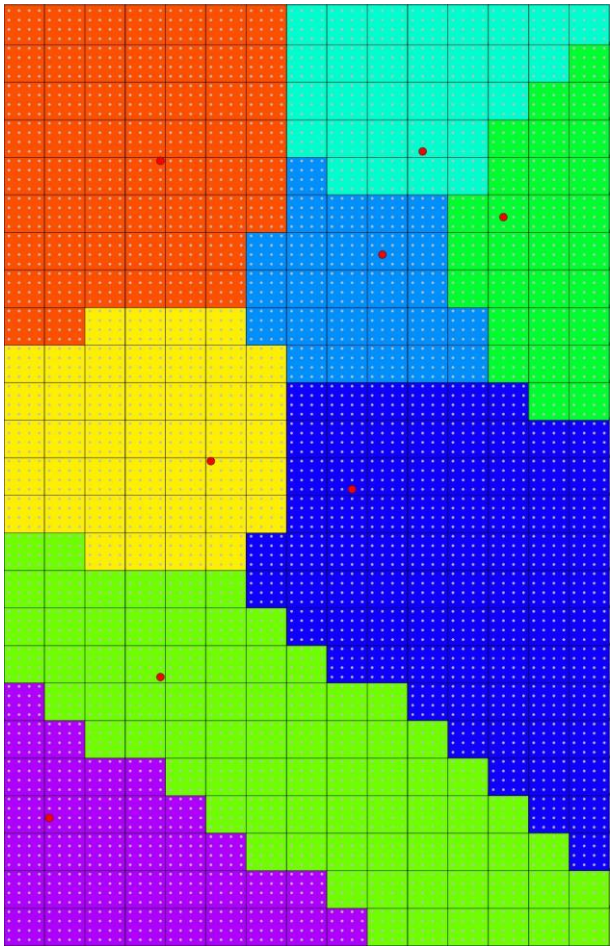

**Figure 1.** Image of the Voronoi partition

The whole rectangle represents a fault zone, and small squares represent sub-faults. Red circles represent the Voronoi nuclei, and gray dots represent nucleus grid points (i.e., candidates for the Voronoi nuclei). The colors of sub-faults indicate extents of the Voronoi cells classified by the Voronoi nuclei.

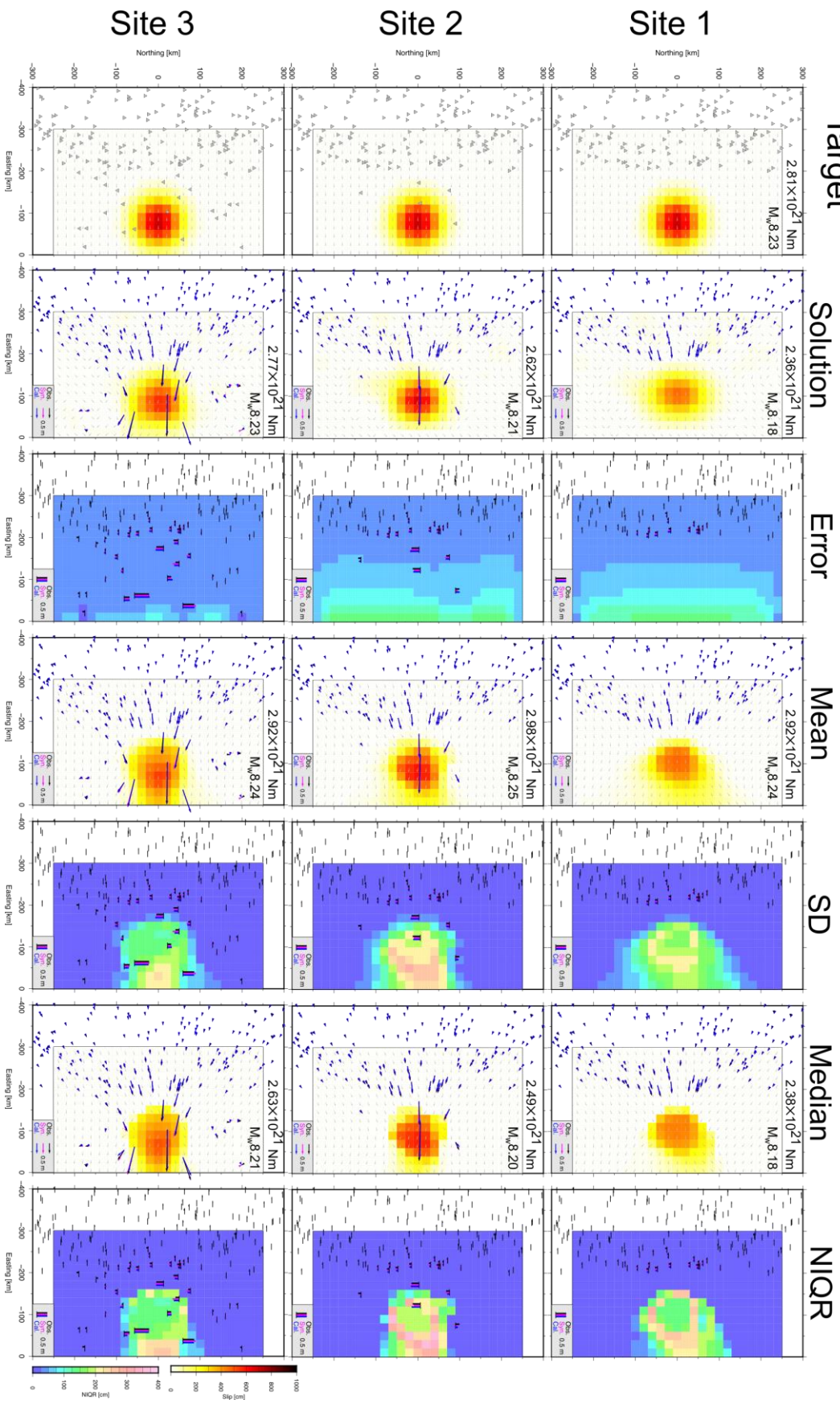
Site 3
Site 2
Site 1
Target
ABIC-LSM
Solution
Error
Mean
Rj-MCMC
SD
Median
NIQR
Northing [km]
Easting [km]
2.81×10^21 Nm
Mw8.23
2.36×10^21 Nm
Mw8.18
2.62×10^21 Nm
Mw8.21
2.77×10^21 Nm
Mw8.23
2.92×10^21 Nm
Mw8.24
2.98×10^21 Nm
Mw8.25
2.92×10^21 Nm
Mw8.24
2.38×10^21 Nm
Mw8.18
2.49×10^21 Nm
Mw8.20
2.63×10^21 Nm
Mw8.21
Obs.
Cal.
0.5 m
NIQR [cm]
Slip [cm]

**Figure 2**. The estimated slip distributions and the estimation errors of synthetic test 1

The upper, middle, and lower panels show results of the synthetic test 1 assuming the site patterns 1, 2, and 3, respectively. Leftmost panels show the target slip distribution, and triangles and inverse triangles indicate synthetic onshore and offshore geodetic sites. The other panels show the estimated slip distributions and the estimation error distributions given by the ABIC-LSM and the rj-MCMC method (the mean and median models). Magenta, black, and blue vectors in the estimated slip distributions indicate the synthetic, and observed (synthetic displacements with observational noises), and calculated displacements in the horizontal components, respectively. The bars in the estimation error distribution indicate the displacements in the vertical component. Colors of the bars indicate the same meanings with the vectors.

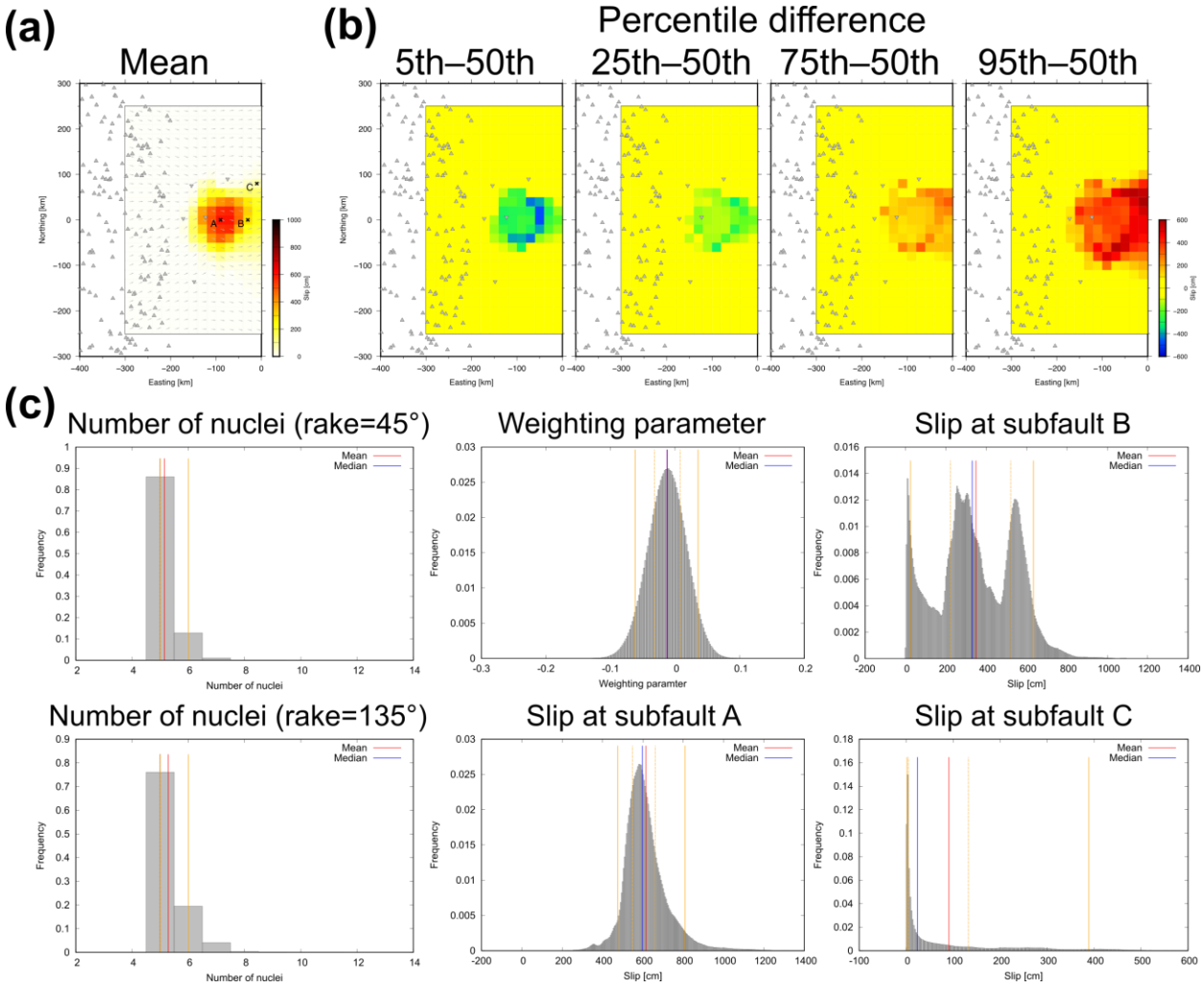


**Figure 3**. The percentile differences and the histograms for the synthetic test 1 assuming the site pattern 2

(a) The slip distribution estimated by the rj-MCMC method (the mean model) with the site distribution as shown in Figure 2. (b) The slip distributions for percentiles of 5th, 25th, 75th, and 95th subtracting 50th percentile (the median model). (c) The histograms for unknowns: number of the Voronoi nuclei for the fault slip component of rake=45°, that of rake=135°, the weighting parameter, and slips at sub-fault A, B, and C shown in (a). The vertical axis of each histogram indicate sample's frequency (i.e., number of the samples at certain range over total number of the samples). Red and blue vertical lines represent mean and median values, respectively. Solid orange vertical lines represent 5th and 95th percentile values, and dotted orange vertical lines represent 25th and 75th percentile values.

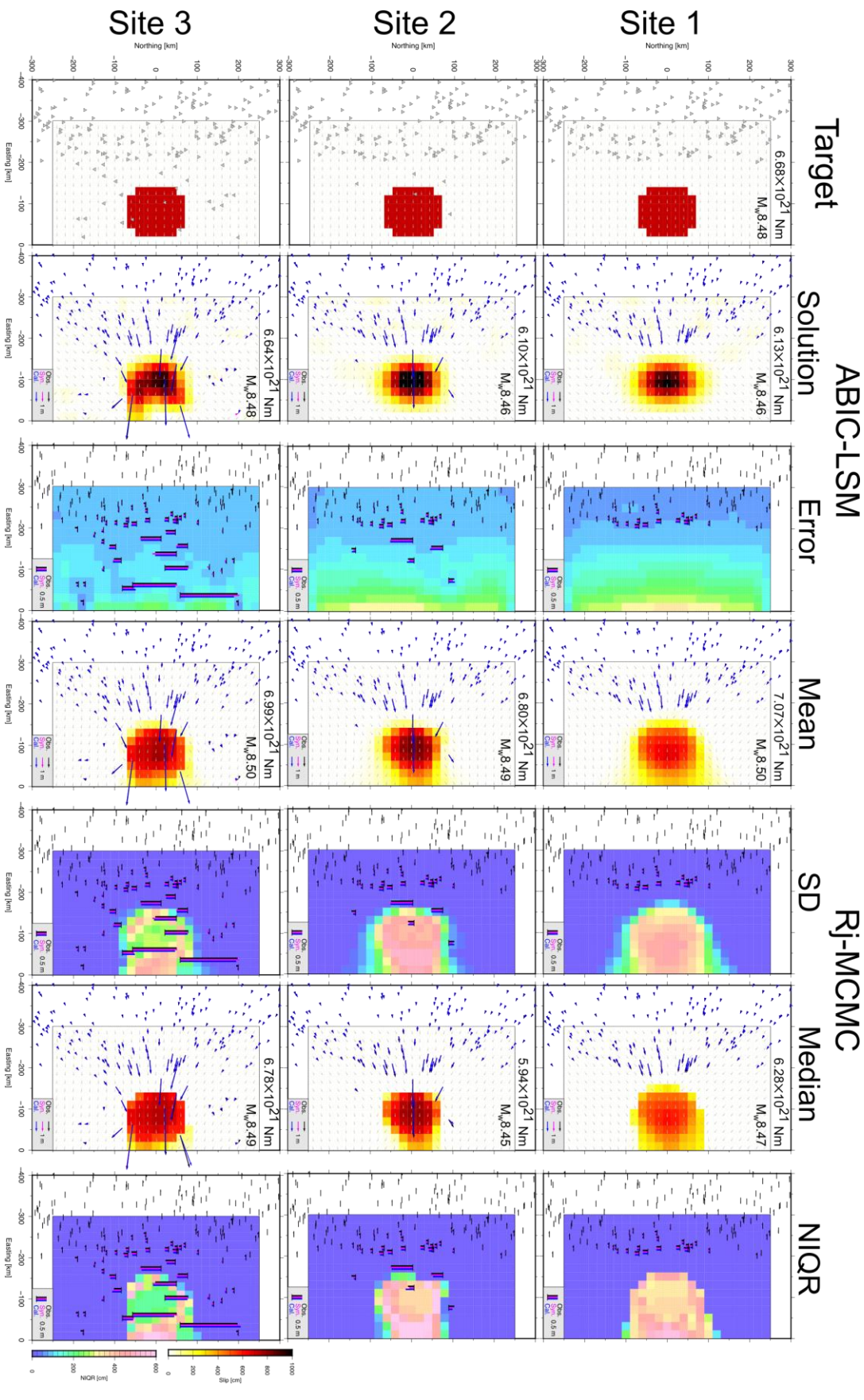
Site 3
Site 2
Site 1
Target
ABIC-LSM
Solution
Error
Mean
Rj-MCMC
SD
Median
NIQR
Northing [km]
Easting [km]
6.68×10^21 Nm
Mw8.48
6.64×10^21 Nm
Mw8.48
6.13×10^21 Nm
Mw8.46
6.10×10^21 Nm
Mw8.46
7.07×10^21 Nm
Mw8.50
6.80×10^21 Nm
Mw8.49
6.99×10^21 Nm
Mw8.50
6.28×10^21 Nm
Mw8.47
5.94×10^21 Nm
Mw8.45
6.78×10^21 Nm
Mw8.49
Obs.
Cal.
1 m
0.5 m
NIQR [cm]
Slip [cm]

**Figure 4**. The estimated slip distributions and the estimation errors of synthetic test 2
The panels show results of the synthetic test 2 in the same manner as Figure 2.

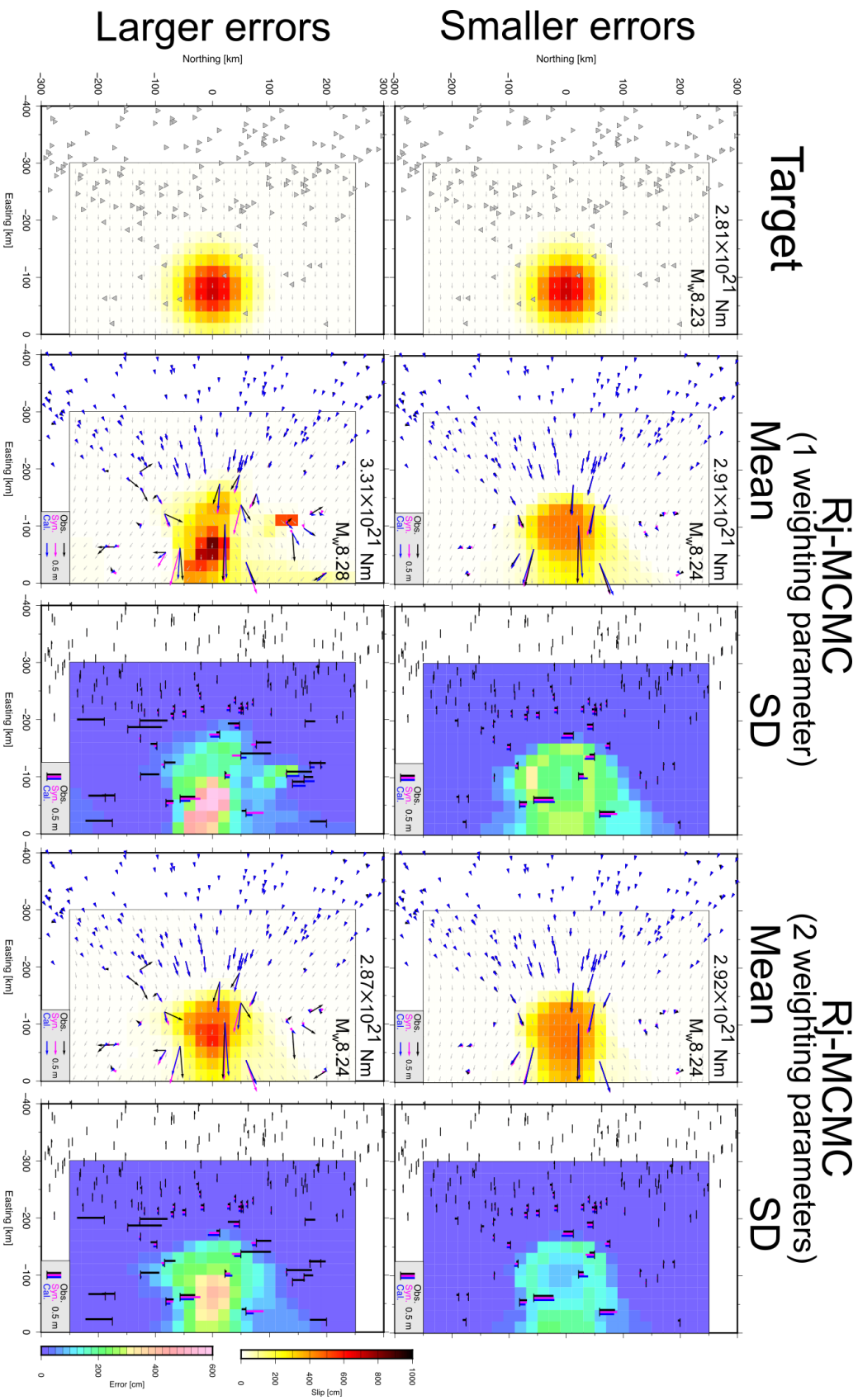
Larger errors
Smaller errors
Target
Rj-MCMC (1 weighting parameter) Mean
SD
Rj-MCMC (2 weighting parameters) Mean
SD
2.81×10^21 Nm Mw8.23
2.91×10^21 Nm Mw8.24
3.31×10^21 Nm Mw8.28
2.92×10^21 Nm Mw8.24
2.87×10^21 Nm Mw8.24
Northing [km]
Easting [km]
Obs.
Syn.
Cal.
0.5 m
Error [cm]
Slip [cm]

939

940 **Figure 5**. The estimated slip distributions and the estimation errors of synthetic test 3

941 The upper and lower panels show results of the synthetic test 3 assuming the smaller and
942 larger error cases, respectively. Leftmost panels show the target slip distribution, and triangles
943 and inverse triangles represent the same with Figure 2. The second and third columns show the
944 estimated slip distributions and the estimation error distributions given by the rj-MCMC method
945 with single weighting parameter, respectively. The fourth and fifth columns show the estimation
946 results given by the rj-MCMC method with dual weighting parameter. The vectors and bars are
947 written in the same manner as Figure 2.

948

949

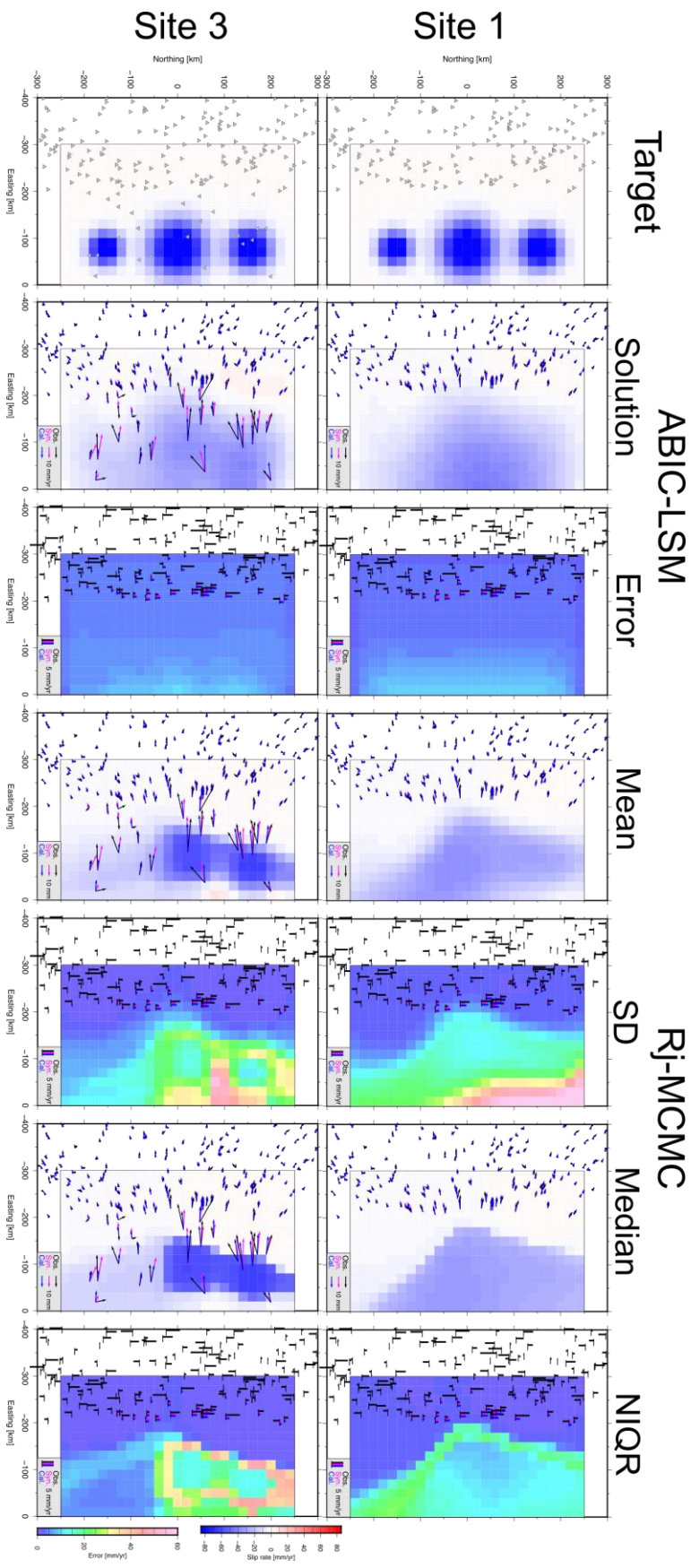
Site 3
Site 1
Northing [km]
Easting [km]
Target
ABIC-LSM
Solution
Error
Mean
Rj-MCMC
SD
Median
NIQR
Obs.
Cal.
Error [mm/yr]
Slip rate [mm/yr]

950

951
952 **Figure 6**. The estimated slip distributions and the estimation errors of synthetic test 4
953 The upper and lower panels show results of the synthetic test 4 assuming the site patterns
954 1 and 3, respectively. The panels for each column show the results in the same manner as Figure
955 2.
956
957
958
959

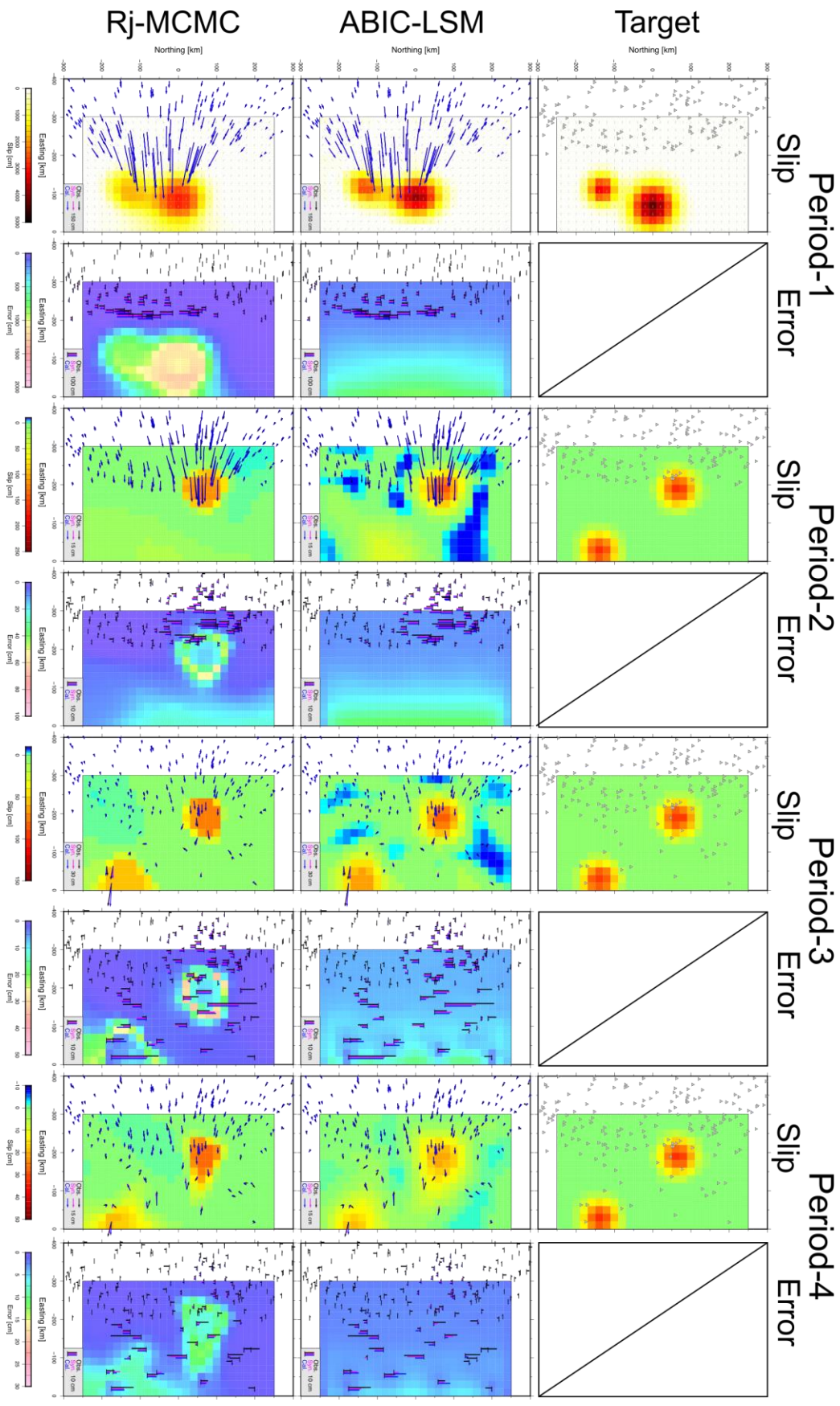
Rj-MCMC
ABIC-LSM
Target
Northing [km]
Easting [km]
Slip [cm]
Error [cm]
Period-1
Slip
Error
Period-2
Slip
Error
Period-3
Slip
Error
Period-4
Slip
Error

961

962 **Figure 7**. The estimated slip distributions and the estimation errors of synthetic test 5

963 The panels for each row show the target slip distributions and the estimation results for
964 the periods 1–4. The upper panels show the target slip distributions. The middle and lower panels
965 show results of the synthetic test 5 estimated by the ABIC-LSM and the rj-MCMC method,
966 respectively. The vectors and bars are written in the same manner as Figure 2.

967

968

969

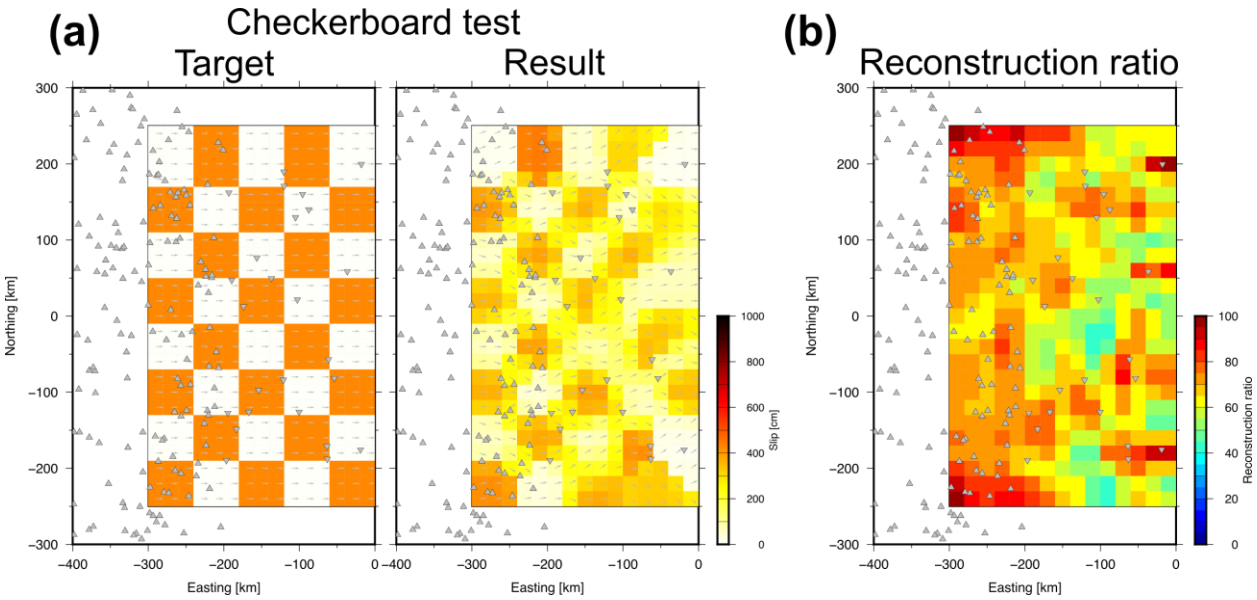


970

971 **Figure 8**. Example of the checkerboard resolution test and reconstruction ratio for the synthetic
972 test 1

973 (a) The target and estimated slip distributions for one pattern of the checkerboard
974 resolution tests. Triangles and inverse triangles represent the same with Figure 2. (b) Map of the
975 reconstruction ratio averaging all patterns of the checkerboard resolution tests.

976

977

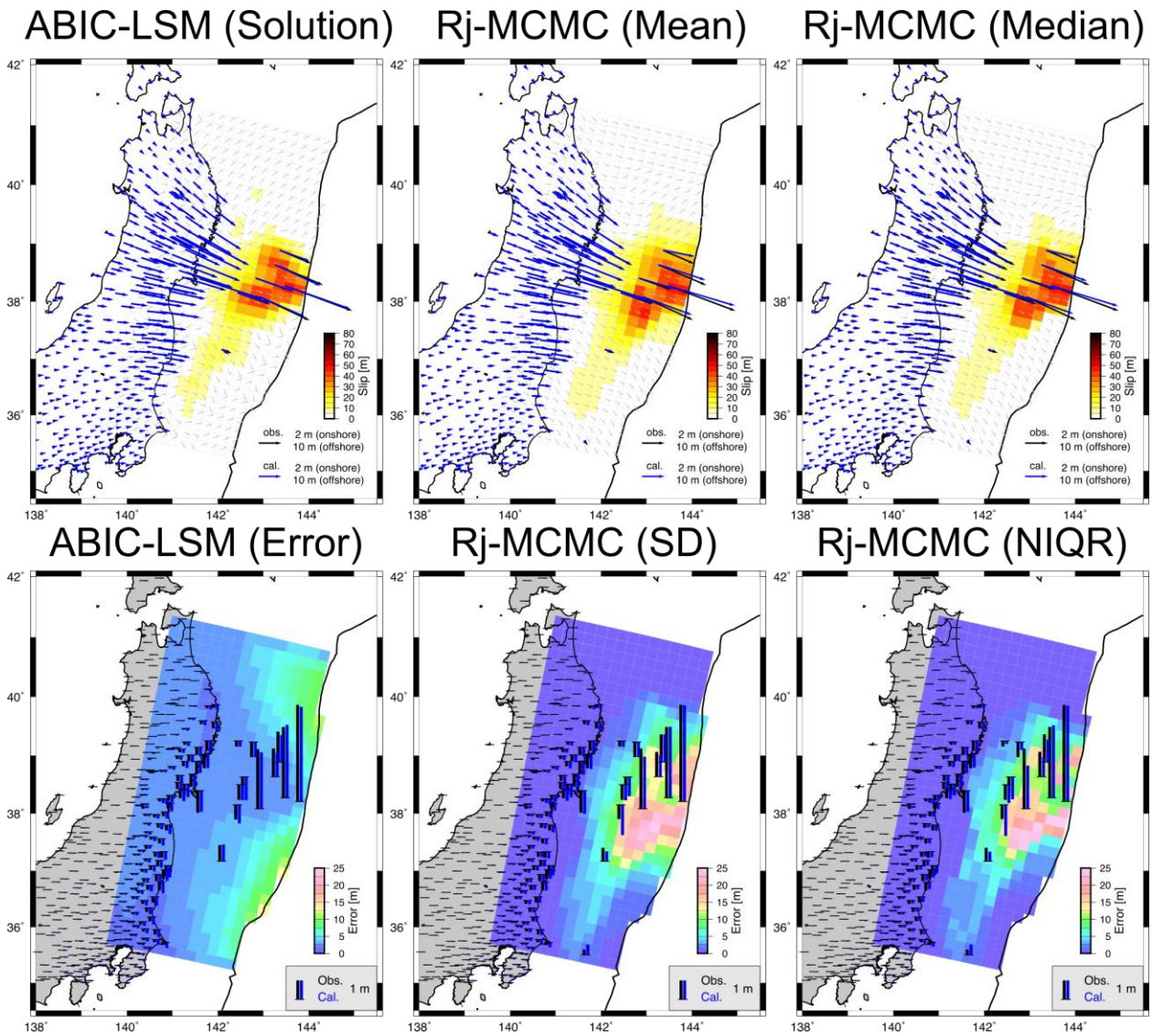


**Figure 9**. The estimated slip distributions and the estimation errors of the application

The upper and lower panels show the estimated slip distributions and the estimation error distributions of the 2011 Tohoku-oki earthquake, respectively. The first, second, and third rows show the results of the ABIC-LSM solution, the mean model of the rj-MCMC method, and the median model of the rj-MCMC method, respectively. The black and blue vectors represent the observed and calculated displacements in the horizontal components, respectively. The black and blue bars represent the observed and calculated displacements in the vertical component, respectively.

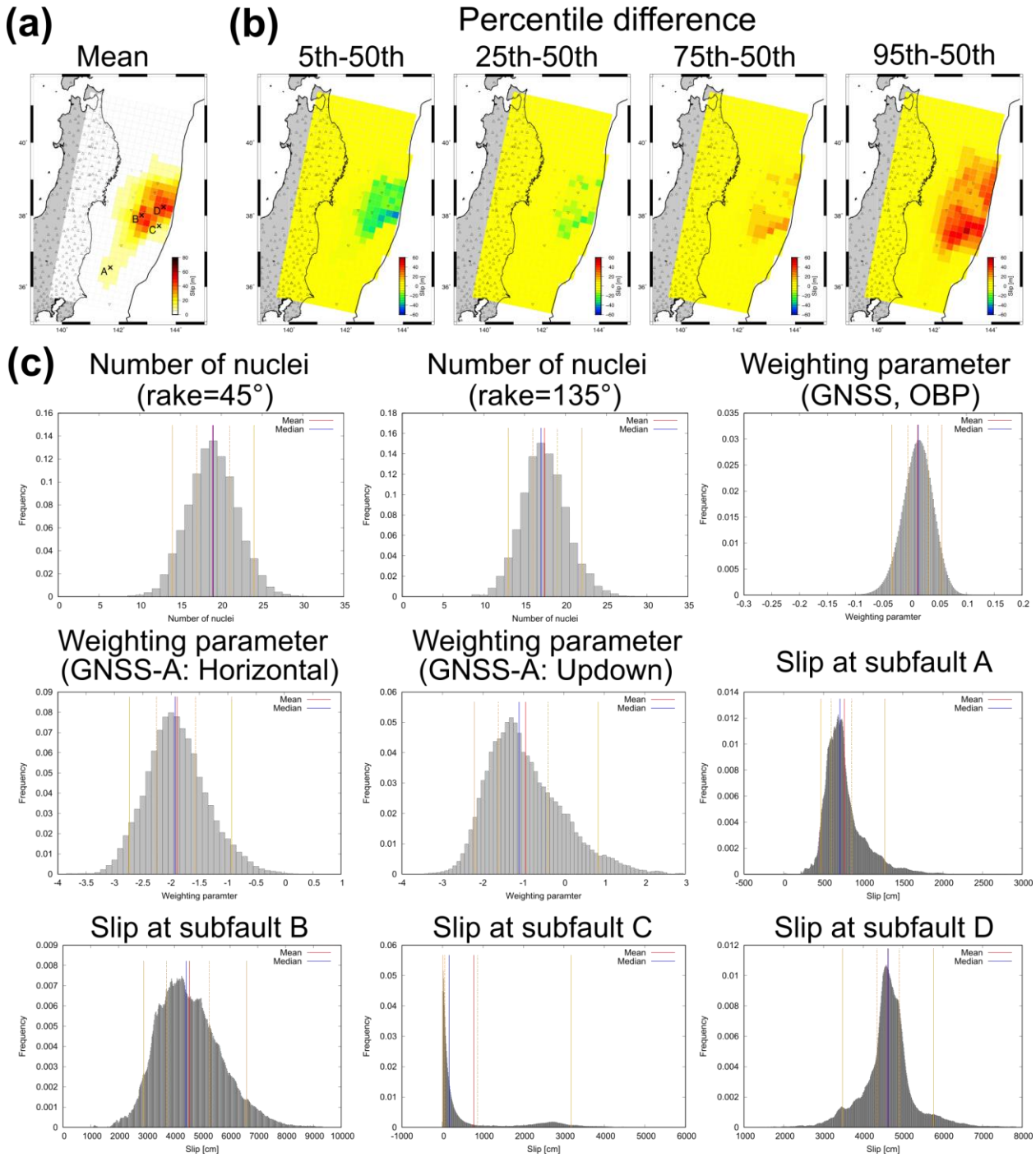


**Figure 10**. The percentile differences and the histograms for the application

(a) The slip distribution estimated by the rj-MCMC method (the mean model) with the site distribution as shown in Figure 9. (b) The panels show the percentile differences as the same manner with Figure 3. (c) The histograms for unknowns: number of the Voronoi nuclei for the

fault slip component of rake=45°, that of rake=135°, the weighting parameters, and slips at sub-fault A, B, C, and D shown in (a). The histograms are expressed in the same manner as Figure 3.

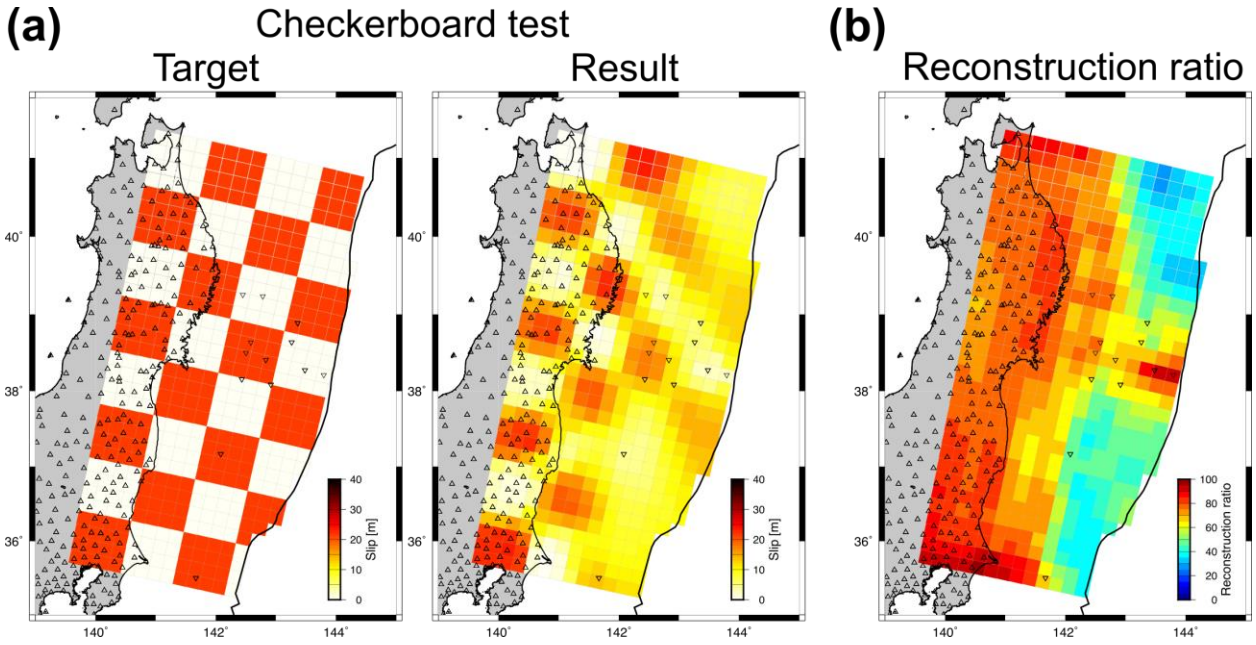


**Figure 11**. Example of the checkerboard resolution test and reconstruction ratio for the 2011 Tohoku-oki earthquake

(a) The target and estimated slip distributions for one pattern of the checkerboard resolution tests. (b) Map of the reconstruction ratio averaging all patterns of the checkerboard resolution tests.